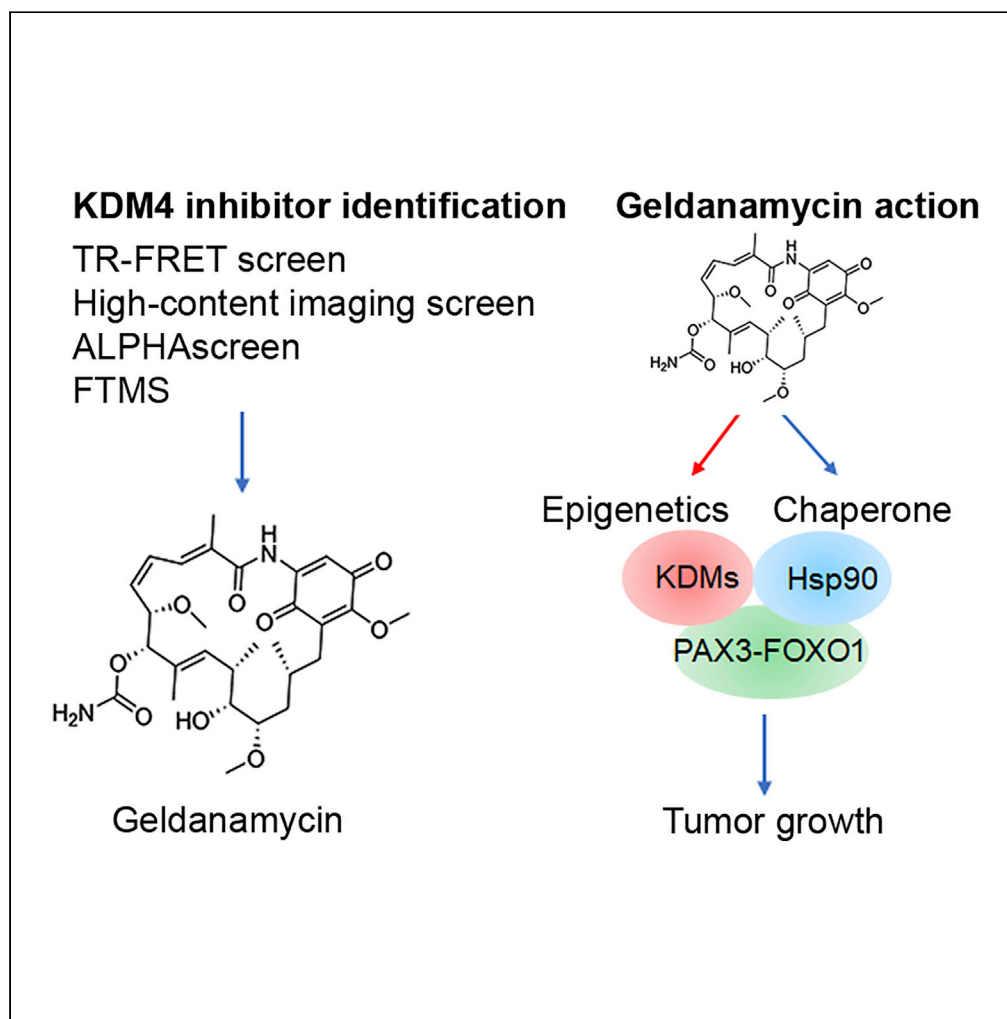


## Article

## 17-DMAG dually inhibits Hsp90 and histone lysine demethylases in alveolar rhabdomyosarcoma



Shivendra Singh,  
Ahmed Abu-Zaid,  
Wenwei Lin, ...,  
Andrew M.  
Davidoff,  
Taosheng Chen,  
Jun Yang

taosheng.chen@stjude.org  
(T.C.)  
jun.yang2@stjude.org (J.Y.)

**Highlights**

Identification of  
geldanamycin/17-DMAG  
as histone lysine  
demethylase inhibitors

Geldanamycin/17-DMAG  
causes degradation of  
PAX3-FOXO1, an Hsp90  
client

Geldanamycin/17-DMAG  
induces epigenetic  
changes and targets  
PAX3-FOXO1 pathway

17-DMAG alone or  
combined with  
chemotherapy show  
potency to PAX3-FOXO1  
xenografts

Singh et al., iScience 24,  
101996  
January 22, 2021 © 2020 The  
Author(s).  
[https://doi.org/10.1016/  
j.isci.2020.101996](https://doi.org/10.1016/j.isci.2020.101996)

## Article

## 17-DMAG dually inhibits Hsp90 and histone lysine demethylases in alveolar rhabdomyosarcoma

Shivendra Singh,<sup>1,9</sup> Ahmed Abu-Zaid,<sup>1,9</sup> Wenwei Lin,<sup>2,9</sup> Jonathan Low,<sup>2</sup> Alireza Abdolvahabi,<sup>2</sup> Hongjian Jin,<sup>8</sup> Qiong Wu,<sup>1</sup> Bailey Cooke,<sup>1</sup> Jie Fang,<sup>1</sup> John Bowling,<sup>2</sup> Sivaraja Vaithiyalingam,<sup>3,4</sup> Duane Currier,<sup>2</sup> Mi-Kyung Yun,<sup>4</sup> Dinesh M. Fernando,<sup>2</sup> Julie Maier,<sup>2</sup> Heather Tillman,<sup>5</sup> Purva Bulsara,<sup>6</sup> Zhaohua Lu,<sup>6</sup> Sourav Das,<sup>2</sup> Anang Shelat,<sup>2</sup> Zhenmei Li,<sup>4</sup> Brandon Young,<sup>2</sup> Richard Lee,<sup>2</sup> Zoran Rankovic,<sup>2</sup> Andrew J. Murphy,<sup>1</sup> Stephen W. White,<sup>4,7</sup> Andrew M. Davidoff,<sup>1</sup> Taosheng Chen,<sup>2,\*</sup> and Jun Yang<sup>1,10,\*</sup>

## Summary

**Histone lysine demethylases (KDMs) play critical roles in oncogenesis and therefore may be effective targets for anticancer therapy. Using a time-resolved fluorescence resonance energy transfer demethylation screen assay, in combination with multiple orthogonal validation approaches, we identified geldanamycin and its analog 17-DMAG as KDM inhibitors. In addition, we found that these Hsp90 inhibitors increase degradation of the alveolar rhabdomyosarcoma (aRMS) driver oncoprotein PAX3-FOXO1 and induce the repressive epigenetic mark H3K9me3 and H3K36me3 at genomic loci of PAX3-FOXO1 targets. We found that as monotherapy 17-DMAG significantly inhibits expression of PAX3-FOXO1 target genes and multiple oncogenic pathways, induces a muscle differentiation signature, delays tumor growth and extends survival in aRMS xenograft mouse models. The combination of 17-DMAG with conventional chemotherapy significantly enhances therapeutic efficacy, indicating that targeting KDM in combination with chemotherapy may serve as a therapeutic approach to PAX3-FOXO1-positive aRMS.**

## Introduction

Histone lysine methylation mediates multiple important biological processes including DNA replication, DNA repair, and gene expression (Greer and Shi, 2012; Martin and Zhang, 2005; Rodriguez-Paredes and Esteller, 2011). Histone methylation was initially felt to be irreversible until lysine-specific demethylase 1 (LSD1, KDM1A) was identified (Shi et al., 2004). Subsequent studies identified another family of histone demethylases, Jumonji C (JmjC) domain-containing demethylases (Hojfeldt et al., 2013), which requires iron and 2-oxoglutarate for their activities. The JmjC histone lysine demethylases (KDMs) are composed of 17 members and are responsible for reversing most of the histone methyl marks in the human epigenome. Aberrant histone lysine methylation is commonly seen in a variety of cancers (Esteller, 2008), due to genetic alteration or dysregulated expression of histone lysine methyltransferases and KDMs (Chi et al., 2010; Hojfeldt et al., 2013; Huether et al., 2014; Kandoth et al., 2013; Shi, 2007; Shi and Whetstone, 2007).

The KDM4 (KDM4A-D) subfamily are Jumonji-domain containing KDMs which are responsible for removing methyl groups from tri- and dimethylated H3K9 and H3K36 (H3K9me2/me3, H3K36me2/me3) (Kooistra and Helin, 2012). KDM4B is particularly important as it is involved in a variety of physiological functions (Wilson and Krieg, 2019). It regulates DNA repair (Young et al., 2013), self-renewal of embryonic stem cells (Das et al., 2014), conversion of induced pluripotent stem cells (Chen et al., 2013), osteogenic differentiation (Ye et al., 2012), obesity (Cheng et al., 2018), and mammary development (Kawazu et al., 2011). KDM4B is also involved in regulation of copy number gain at specific chromosomal loci (Mishra et al., 2018), topoisomerase-II accessibility to chromatin (Seoane et al., 2019) and demethylation of non-histone proteins such as AKT (Guo et al., 2019). We and others have shown that KDM4B is a direct target of estrogen receptor alpha (ER $\alpha$ ) and hypoxia-inducible factor 1 (HIF1) in ER $\alpha$ <sup>+</sup> breast cancer (Hahm et al., 2011; Kawazu et al., 2011; Yang et al., 2009, 2010), and that it

<sup>1</sup>Department of Surgery, St Jude Children's Research Hospital, 262 Danny Thomas Place, Memphis TN 38105, USA

<sup>2</sup>Department of Chemical Biology and Therapeutics, St Jude Children's Research Hospital, 262 Danny Thomas Place, Memphis, TN 38105, USA

<sup>3</sup>Protein Technologies Center, St Jude Children's Research Hospital, 262 Danny Thomas Place, Memphis, TN 38105, USA

<sup>4</sup>Department of Structural Biology, St Jude Children's Research Hospital, 262 Danny Thomas Place, Memphis, TN 38105, USA

<sup>5</sup>Department of Pathology, St Jude Children's Research Hospital, 262 Danny Thomas Place, Memphis, TN 38105, USA

<sup>6</sup>Department of Biostatistics, St Jude Children's Research Hospital, 262 Danny Thomas Place, Memphis, TN 38105, USA

<sup>7</sup>Graduate School of Biomedical Sciences, St Jude Children's Research Hospital, 262 Danny Thomas Place, Memphis, TN 38105, USA

<sup>8</sup>Center for Applied Bioinformatics, St Jude Children's Research Hospital, 262 Danny Thomas Place, Memphis, TN 38105, USA

<sup>9</sup>These authors contributed equally

<sup>10</sup>Lead contact

\*Correspondence: taosheng.chen@stjude.org (T.C.), jun.yang2@stjude.org (J.Y.)  
<https://doi.org/10.1016/j.isci.2020.101996>



epigenetically regulates G2/M phase cell cycle gene expression (Yang et al., 2010). In addition, KDM4B is a key molecule in androgen receptor signaling in prostate cancer (Coffey et al., 2013; Duan et al., 2019). Recently, we further showed that KDM4B is involved in neuroblastoma growth and tumor maintenance (Yang et al., 2015). Another study has shown that KDM4B is involved in the regulation of unfolded protein response (UPR) in *PTEN*-deficient triple-negative breast cancers, and genetic depletion or small molecule inhibition of KDM4B activates the UPR pathway, resulting in preferential apoptosis (Wang et al., 2018). These data indicate that KDM4B is a potential target for cancer therapy and so several groups, including us, have attempted to develop KDM4 inhibitors (Chen et al., 2017; Chu et al., 2014; Duan et al., 2015; King et al., 2010; Yang et al., 2017). We previously identified ciclopirox as a KDM4B inhibitor that has antitumor activity (Yang et al., 2017), targeting the Myc pathway and inducing neuroblastoma differentiation. Unfortunately, however, ciclopirox has poor *in vivo* pharmacokinetics. To develop more potent KDM4B inhibitors that are suitable for *in vivo* treatment, we employed multiple orthogonal validation approaches, and identified the Hsp90 inhibitors, geldanamycin and its analog 17-dimethylaminoethylamino-17-demethoxy-geldanamycin (17-DMAG) (Jez et al., 2003; Whitesell et al., 1994), as potent KDM4B inhibitors. Geldanamycin inhibited KDMs enzymatic activity, leading to an increase of the repressive transcription mark H3K9me<sub>3</sub>, at multiple target gene loci of PAX3-FOXO1, an oncogenic fusion oncoprotein that drives clinically unfavorable alveolar rhabdomyosarcoma (aRMS). We also found that PAX3-FOXO1 is an Hsp90 client, and is destabilized by geldanamycin and 17-DMAG. In contrast to other reported Hsp90 inhibitors (Kang et al., 2012; Lock et al., 2013), 17-DMAG significantly delayed tumor growth of PAX3-FOXO1 aRMS, affected multiple oncogenic pathways, and induced a muscle differentiation signature. The combination of 17-DMAG with conventional chemotherapy further enhanced antitumor efficacy in mouse xenograft models, indicating that targeting KDMs in combination with chemotherapy may serve as a therapeutic approach to PAX3-FOXO1-positive aRMS.

## Results

### TR-FRET demethylation assay identifies geldanamycin as a potent KDM4B inhibitor

We developed a primary screening, time-resolved fluorescence resonance energy transfer (TR-FRET) demethylation functional assay, to identify novel KDM4B inhibitors (Figure 1A). While KDM4A-4C are known to demethylate both H3K9me<sub>3</sub> and H3K36me<sub>3</sub>, *in vitro* kinetic studies showed that KDM4A-4C are less efficient to demethylate H3K36me<sub>3</sub> (Hillringhaus et al., 2011). Thus, H3K36me<sub>3</sub> may not be a good KDM4 substrate *in vitro* for a TR FRET assay. The assay uses a Terbium (Tb)-labeled anti-H3K9me<sub>2</sub> antibody as a fluorescence donor, and an AF488 tagged streptavidin as a fluorescence acceptor that detects the biotinylated histone H3K9me<sub>2</sub> peptide. When uninhibited, KDM4B converts the substrate H3K9me<sub>3</sub> peptide to the product H3K9me<sub>2</sub> peptide, which is recognized and bound by both the donor Tb-labeled antibody and acceptor AF488-labeled streptavidin. The resulting proximity of the Tb donor and the AF488 acceptor elicits a fluorescence emission at 520 nm when excited at 340 nm. When the KDM4B activity is inhibited, less biotin-H3K9me<sub>2</sub> is generated and the 520 nm emission signal (and the 520 nm/490 nm ratio) is reduced. We optimized the conditions by (1) confirmation of the specificity of the Tb-labeled anti-H3K9me<sub>2</sub> antibody to the Biotin-H3K9me<sub>2</sub> peptide among the 4 relevant peptides (Biotin-H3K9me<sub>0</sub>, Biotin-H3K9me<sub>1</sub>, Biotin-H3K9me<sub>2</sub> and Biotin-H3K9me<sub>3</sub>), (2) confirmation of the specificity of Tb-anti-H3K9me<sub>2</sub> antibody to the product Biotin-H3K9me<sub>2</sub> peptide over the substrate Biotin-H3K9me<sub>3</sub> peptide over a wide concentration range (0.3 nM–312.5 nM), (3) optimization of the KDM4B concentrations, (4) optimization of incubation time, (5) optimization of KDM4B activity in three selected buffers, (6) optimization of the salt types and their concentrations in buffers, and (7) evaluation of DMSO tolerance of the assay (Figure S1). Our TR-FRET assay displayed predictability and reproducibility of responses to known KDM4B inhibitors and showed a clear threshold between positive and negative responses (Figures 1B and 1C). The high-throughput screening (HTS) statistical parameter Z'(Z-prime) had an average value of 0.73 (0.55–0.87) from our pilot screen (Figure 1D), indicating that the assay is robust and reproducible. On the basis of the optimized parameters, we performed a pilot screening of 3262 FDA-approved drugs and bioactive molecules and identified the Hsp90 inhibitor geldanamycin, a member of ansamycin family molecules, as a potent KDM4B inhibitor with an IC<sub>50</sub> of 50.1 nM (Figures 1E and 1F).

In the screening library, there were other non-ansamycin Hsp90 inhibitors (Ganetespib, KW2478, SNX-5422, AT13387, NVP-AUY922, STA-4783 and XL888). However, none of them showed an activity >15% of inhibition to KDM4B (Figure S2). Because the KDM4B inhibitory activities of these non-ansamycin Hsp90 inhibitors were relatively low (%Inhibition <15% at 15 μM), they were not further tested in the dose response confirmation.

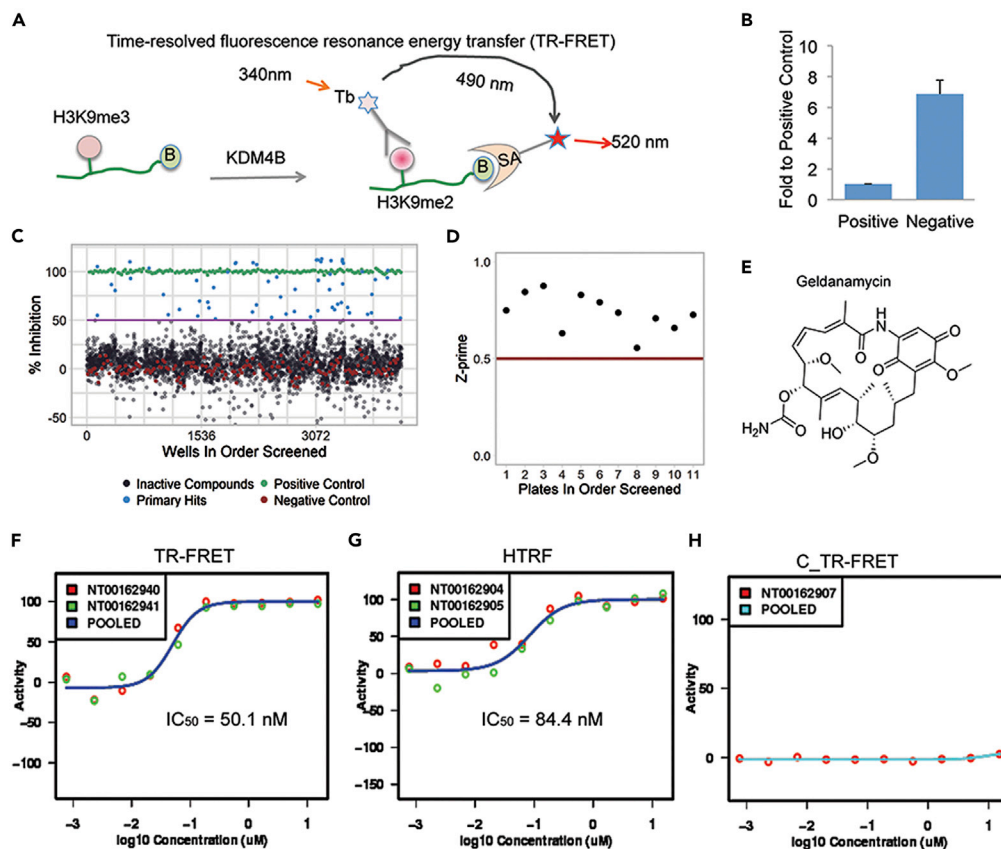


**Figure 1. Identification of geldanamycin as a potent KDM4B inhibitor**

(A) The KDM4B TR-FRET demethylation functional assay: As a KDM4B substrate, the Biotin-linked H3K9me3 peptide is converted to the product Biotin-H3K9me2 peptide, which is bound by both the Terbium-labeled anti-H3K9me2 antibody and AF488-streptavidin and brings the donor fluorophore Tb and acceptor fluorophore AF488 into close proximity. A high TR-FRET signal in the form of light emission at 520 nm from the acceptor fluorophore AF488 is generated when the donor fluorophore Tb was excited at 340 nm. (B = biotin, SA = streptavidin, Tb = Terbium).

(B) Fold ratio between positive and negative controls from the validation assay. The positive control is the group without KDM4B protein (mimic 100% inhibition) and the negative control is the group with 750 nM in-house KDM4B protein (mimic 0% inhibition).

(C) Activity scatterplot of all compounds tested in the TR-FRET assay (Green: positive control; Blue: primary hits; Black: inactive compounds; Red: negative control).

(D) Z-prime factor from the screen. The Z-prime factor value was calculated using the Equation 1 for each plate based on the method reported in the literature (Zhang et al., 1999). Each dot represents Z-prime factor value for one assay plate.

(E) The chemical structure of geldanamycin.

(F) Representative TR-FRET dose-response inhibitory activity curve of geldanamycin against KDM4B. Red dots are activity values of geldanamycin at its respective concentrations in the assay plate of NT00162940. Green dots are activity values of geldanamycin at its respective concentrations in the assay plate of NT00162941. Blue curve is the dose-response curve derived from the average inhibitory activities or pooled activities of geldanamycin at its corresponding concentrations. (G) Representative HTRF dose-response inhibitory activity curve of geldanamycin against KDM4B. Red dots are activity values of geldanamycin at its respective concentrations in the assay plate of NT00162904. Green dots are activity values of geldanamycin at its respective concentrations in the assay plate of NT00162905. Blue curve is the dose-response curve derived from the average inhibitory activities or pooled activities of geldanamycin at its corresponding concentrations. (H) Representative background TR-FRET dose-response curve of geldanamycin without KDM4B protein. Red dots are activity values of geldanamycin at its respective concentrations in the assay plate of NT00162907. Green curve is the dose-response curve derived from the inhibitory activities or pooled activities of geldanamycin at its corresponding concentrations.

See also Figures S1 and S2.

We also designed a homogeneous TR-FRET assay (HTRF) that is similar to TR-FRET, but the fluorophore AF488 is replaced with AF647, which switches the light detection wavelength from 520 nm to 665 nm to avoid interference by intrinsically fluorescent compounds and reduce false positives. The HTRF assay obtained a comparable  $IC_{50}$  value (84.4 nM) for geldanamycin (Figure 1G). Omitting KDM4B abrogated the drug response relationship, confirming that inhibition of KDM4B-mediated conversion of H3K9me3 to H3K9me2 by geldanamycin appears to be KDM4B-mediated (Figure 1H).

### Orthogonal identification of geldanamycin as a KDM4B inhibitor by high-content immunofluorescence imaging and a matrix-assisted laser desorption/ionization-Fourier transform ion cyclotron resonance (MALDI-FTICR) mass spectrometry-based approach

We also developed an orthogonal phenotypic assay in parallel with the TR-FRET assay as a validation approach. We made a retroviral vector to transfer the wild-type KDM4B gene and a catalytically dead mutant of KDM4B (H189A), in which histidine 189 was replaced by alanine, resulting in the loss of iron binding activity, leading to the loss of demethylation function. We then transduced U2OS cells with these retroviral vectors (Figure 2A), as this osteosarcoma cell line was able to tolerate overexpression of KDM4B and the differential H3K9me3 signals can be easily detected by microscope. We monitored the H3K9me3 levels with immunofluorescence imaging. We again found that geldanamycin inhibited KDM4B, with an  $IC_{50}$  of 21.2 nM in this cell-based assay (Figures 2B and 2C). We further assessed the effect of geldanamycin on KDM4B activity via Western blot analysis. 293T cells expressing KDM4B or the catalytically dead mutant were treated with geldanamycin and 17-DMAG, a geldanamycin analog which is better suited for *in vivo* use. Cyclopirox was included as a positive control (Figure S3). Geldanamycin, 17-DMAG, and cyclopirox greatly inhibited KDM4B activity in demethylating H3K9me3 in the cells expressing KDM4B, compared to those expressing the control or catalytically dead mutant (Figure S3). Similar results were obtained in U2OS cells in that geldanamycin and 17-DMAG blocked KDM4B catalytic activity on its H3K9me3 and H3K36me3 substrates but not on H3K4me3, which is not a substrate of KDM4B (Figure 2D). These data indicate that both geldanamycin and its analog 17-DMAG inhibit KDM4B activity in cells.

To further validate geldanamycin as a KDM4B inhibitor, we developed a MALDI-FTICR mass spectrometry-based approach, which is detailed in the [Transparent methods](#). We validated MALDI-FTICR by showing that it was able to detect the KDM4B substrate (H3K9me3) and the product H3K9me2 (Figure 2E). Again, we found that geldanamycin inhibited KDM4B activity with an  $IC_{50}$  of 1.24  $\mu$ M (Figure 2F). Although this method was less sensitive than our TR-FRET and immunofluorescence assays, probably due to the distinct platform and parameters used in this assay, it validated that KDM4B activity was inhibited by geldanamycin *in vitro*.

Microscale Thermophoresis (MST) was employed to measure the binding affinity of geldanamycin with the catalytic domain of KDM4B. MST measures the diffusion of molecules in the response to a microscale temperature change. The diffusion of molecules depends on size, solvation entropy, and surface charge. These properties differ from unbound to bound molecules. Introducing a microscale temperature change induces a difference in fluorescence between unbound and bound target molecules (Seidel et al., 2013). The normalized fluorescence intensities are used to fit the data to extract a binding affinity. A second generation labeling dye was conjugated to the cysteine residues of the KDM4B catalytic domain and geldanamycin was titrated into the labeled protein. Binding of geldanamycin with the catalytic domain of KDM4B revealed a  $K_d$  value of 540 nM (Figure 2G), indicating a direct binding of geldanamycin to the catalytic domain of KDM4B.

### Profiling of geldanamycin and its analogs activity against KDMs using ALPHA screen

To determine the selectivity of geldanamycin against KDMs, a bead-based, non-radioactive Amplified Luminescent Proximity Homogeneous Assay (ALPHA) screen was used to assess the KDM inhibitory activity of geldanamycin at 5  $\mu$ M. We also included geldanamycin analogs 17-DMAG, 17-AAG (17-N-allylamino-17-demethoxy-geldanamycin) and 17-AG (17-Amino Geldanamycin), which is only different at the 17-position of the benzoquinone ring of these compounds (Figure 3A). Geldanamycin showed greatest inhibition to KDM4 and KDM5 subfamilies (Figure 3B), which have the highest sequence homology in comparison to other KDMs with a phylogenetic tree showing that KDM4 and KDM5 members are the closest neighbors (Figure 3B). Interestingly, 17-DMAG had a broader inhibitory activity to KDMs including KDM3-6 (Figure 3B). In contrast, 17-AAG showed a high inhibition to KDM4A and KDM4C but not to KDM4B (Figure 3B). However, another analog, 17-AG, showed activity to KDM4B, KDM4C, KDM5A, and KDM6B but no activity

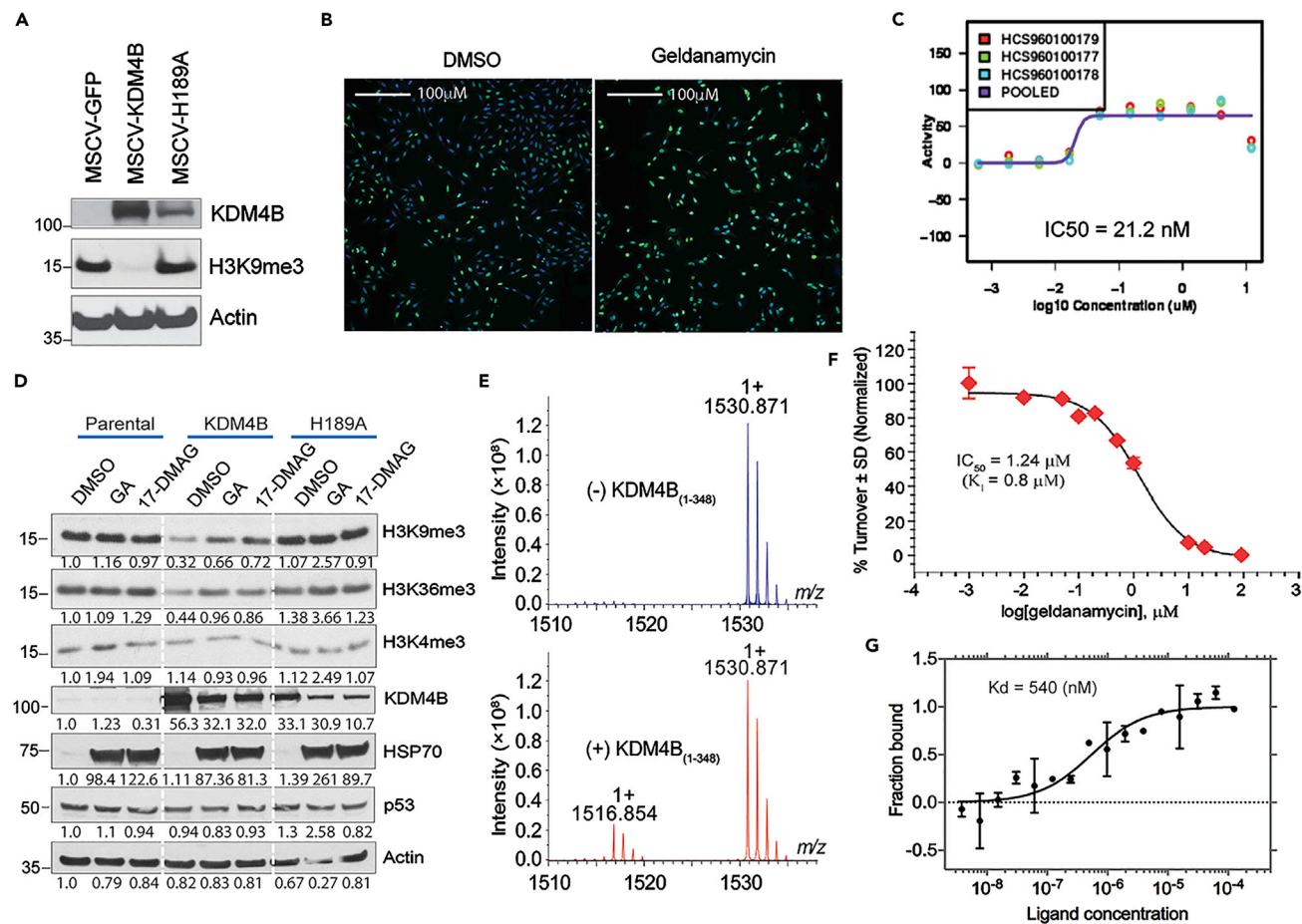


**Figure 2. Orthogonal identification of geldanamycin as a KDM4B inhibitor by high-content immunofluorescence imaging screen and a MALDI-FTICR mass spectrometry-based approach**

(A) Western blot for KDM4B expression in U2OS cells using an anti-KDM4B antibody.

(B) High-content immunofluorescence assay shows geldanamycin inhibits KDM4B activity. The U2OS cells expressing KDM4B were treated with 149nM of geldanamycin for 24 hr. The cells were fixed with 4% formaldehyde and permeabilized with 0.1% Triton X-100, followed by primary anti-H3K9me3 antibody incubation overnight at 4°C. The secondary goat  $\alpha$ -rabbit-Alexa-488 and Hoechst 34,580 were added for imaging. The images were captured of each well at 10X using a GE Healthcare InCell 6,000 at 405nm to detect nuclear staining and 488 nm to detect H3K9me3. Green = H3K9me3, Blue = Hoechst 34,580.

(C) Dose-response curve shows IC50 of KDM4B inhibition by immunofluorescence assay. Purple curve is the dose-response curve derived from the average inhibitory activities or pooled activities of geldanamycin at its corresponding concentrations. Y axis = geldanamycin inhibitory activity; x axis = geldanamycin concentration.

(D) Western blot shows 1 $\mu$ M of geldanamycin (GA) and its analog 17-DMAG block KDM4B activity in U2OS cells, as evidenced by changes in histone methyl marks assessed by specific antibodies, and inhibit the chaperone activity of HSP90 as evidenced by HSP70 compensatory upregulation.

(E) MALDI-FTICR mass spectrometry shows that KDM4B converts H3K9me3 to H3K9me2. Representative mass spectra of histone H3 peptide in the absence (upper panel) and presence (lower panel) of KDM4B.  $m/z = 1530.871$  and  $1516.854$  peaks correspond to trimethylated H3K9 (substrate) and dimethylated H3K9 (product) peptides, respectively. Y axis indicates the signal intensity of H3K9me3 and H3K9me2 peaks.  $m/z$  represents mass divided by charge number and the x axis is expressed in units of  $m/z$ .

(F) Dose-response curve of geldanamycin shows the inhibition of KDM4B with IC50 of 1.24  $\mu$ M, measured by MALDI-FTICR. KDM4B inhibition plot in the presence of geldanamycin. Value for  $K_i$  was calculated upon fitting the plot with Morrison equation. Data are shown as mean  $\pm$  standard deviation ( $n = 3$ ). Y axis indicates the turnover rate of H3K9me3 to H3K9me2, catalyzed by KDM4B. X axis indicates the concentration of geldanamycin.

(G) Microscale Thermophoresis assay of direct binding of KDM4B and geldanamycin. Y axis represents the fractions of KDM4B protein bound by geldanamycin. X axis represents geldanamycin concentration.  $K_d$  = dissociation constant.

to KDM2A and KDM1A (Figure 3B). We further determined the IC<sub>50</sub> of the three ansamycin analogs (Geldanamycin, 17-DMAG and 17-AAG) to KDMs, and we chose 1–2 KDMs that were representatives of each subfamily. Geldanamycin had an IC<sub>50</sub> below 1 $\mu$ M to KDM4B, KDM4C and KDM5A (Figure 3C), while 17-DMAG had an IC<sub>50</sub> below 1 $\mu$ M to KDM3A, KDM4B, KDM4C, KDM5A, and KDM6B (Figure 3C). However, 17-AAG had an IC<sub>50</sub> below 1 $\mu$ M to KDM4C and KDM5A (Figure 3C). All three compounds were much

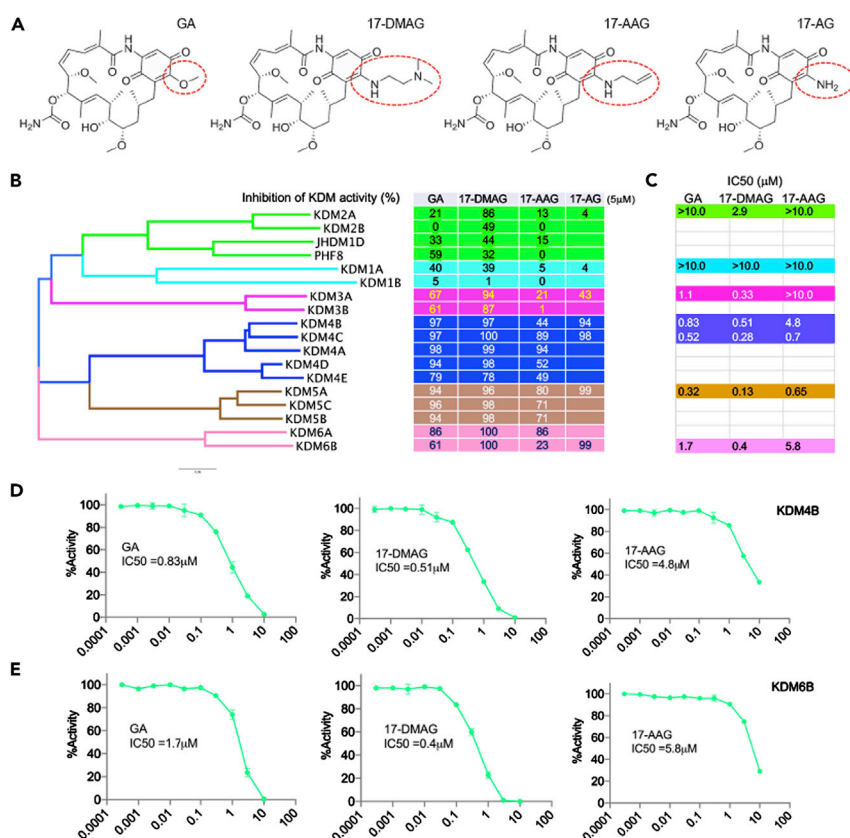


**Figure 3. Profiling of geldanamycin activity against KDMs using ALPHA screen**  
 (A) 17-position of benzoquinone moieties of Geldanamycin, 17-DMAG, 17-AAG and 17-AG are circled (structures were obtained from <https://scifinder.cas.org>).  
 (B) Phylogenetic tree of KDMs (left) and KDM selectivity profiling of geldanamycin, 17-DMAG, 17-AAG AND 17-AG at 5µM (right) assayed by ALPHA Screen.  
 (C) IC<sub>50</sub> of geldanamycin (GA), 17-DMAG and 17-AAG for selected KDMs assayed by ALPHA Screen.  
 (D-E) Dose-response curve of geldanamycin, 17-DMAG and 17-AAG against KDM4B and KDM6B.  
 See also [Figure S3](#).

less effective at inhibiting KDM1A (IC<sub>50</sub> > 10µM), a flavin adenine dinucleotide-dependent amine oxidase domain containing KDM, which is structurally distinct from JmjC KDMs. All three compounds showed a reasonable dose-response relationship ([Figures 3D](#) and [3E](#)). These data indicate that the inhibitory activity of ansamycins to KDMs depends on the specific JmjC domains and is impacted by the modifications at 17-position of the benzoquinone ring of the compounds, which do not inhibit non-JmjC KDMs.

### Geldanamycin and its analog 17-DMAG promotes PAX3-FOXO1 degradation in aRMS cells

Previous studies have shown that Hsp90 also serves to stabilize fusion oncoproteins such as BCR-ABL ([Peng et al., 2007](#)), EML4-ALK ([Richards et al., 2014](#)) and EWS-FLI1 ([Ambati et al., 2014](#)), which have a chaperone dependency as they are Hsp90 clients and are destabilized by Hsp90 inhibitors. Since chimeric oncoproteins do not exist in normal cells, we hypothesized that fusion proteins such as PAX3-FOXO1 might also be more prone to degradation in the absence of cellular Hsp90 chaperone protein function. Therefore, we chose to test the antitumor efficacy of geldanamycin and its analogs in aRMS cell lines which have pathognomonic PAX3-FOXO1 translocation as a driver. We hypothesized that in addition to inhibiting KDM4B, that geldanamycin and 17-DMAG would downregulate PAX3-FOXO1 expression. Indeed, PAX3-FOXO1 expression was reduced by geldanamycin and 17-DMAG ([Figure 4A](#)). Immunoprecipitation confirmed that PAX3-FOXO1 and Hsp90 physically complexed ([Figure 4B](#)). Inhibition of Hsp90 often leads to proteasomal degradation of its clients ([Butler et al., 2015](#)). Consistent with this, the downregulation of PAX3-FOXO1 by geldanamycin or 17-DMAG was rescued by MG132 ([Figure 4C](#)), a reversible proteasome

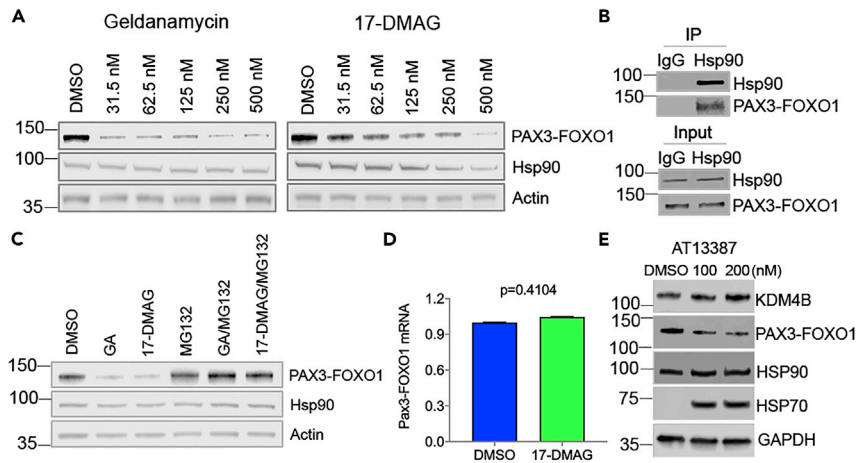


**Figure 4. Geldanamycin promotes PAX3-FOXO1 degradation in aRMS cells**

(A) After 24-hr treatment with geldanamycin or 17-DMAG, Rh30 PAX3-FOXO1 fusion-positive rhabdomyosarcoma cells were lysed for western blotting with the indicated antibodies.  
 (B) Immunoprecipitation of Rh30 cell lysates with mouse IgG or monoclonal Hsp90 antibody, followed by western blotting with indicated antibodies.  
 (C) Rh30 cells were treated with 200nM of geldanamycin or 17-DMAG with or without 5μM of MG132 for 24 hr. Western blot was performed with the indicated antibodies.  
 (D) Quantitative real-time PCR determines the mRNA of PAX3-FOXO1 after 48h treatment of Rh30 cells with 200nM of 17 DMAG (biological triplicates, Student t test). Data are represented as mean ± SEM.  
 (E) The whole cell lysates of Rh30 cells treated with AT13387 for 24 hr are assessed by Western blot with indicated antibodies.

inhibitor. To test if this could be due to alterations in the *PAX3-FOXO1* transcript levels, we performed quantitative PCR using fusion specific primers (spanning the fusion junction) and results showed that *PAX3-FOXO1* gene expression remained unchanged (Figure 4D). We tested the effect of another Hsp90 inhibitor, AT13387, on *PAX3-FOXO1* expression. While this compound showed minimal effect on KDM4B activity (Figure S2), it reduced the expression of *PAX3-FOXO1* (Figure 4E). These data demonstrate that the *PAX3-FOXO1* protein needs Hsp90 for its stabilization, providing the rationale to target *PAX3-FOXO1* protein stability by inhibiting Hsp90 activity. Thus, geldanamycin not only inhibits the enzymatic activity of KDM4B but also downregulates *PAX3-FOXO1* oncoprotein levels by targeting Hsp90, thus making it a unique dual inhibitor.

### Geldanamycin induces the KDM4 substrates H3K9me3 and H3K36me3 in aRMS cancer cells

*PAX3-FOXO1* is a master transcription factor that mainly occupies enhancer regions (Gryder et al., 2017), driving the expression of its downstream target genes such as *FGFR4*, *MYOD1*, and *MYCN*. To test the biological relevance of geldanamycin as a KDM inhibitor in cancer, we treated *PAX3-FOXO1* positive Rh30 cells with geldanamycin and 17-DMAG for 24 hr and assessed changes in the KDM4 substrates H3K9me3 and H3K36me3. Western blot showed that geldanamycin and 17-DMAG induced an increase of H3K9me3 and H3K36me3 (Figure 5A), suggesting that KDM4 activity is inhibited in aRMS cells. We then performed chromatin immunoprecipitation with sequencing (ChIP-seq) to assess the global epigenetic alterations induced by geldanamycin. The results showed that the H3K9me3 and H3K36me3 peaks were profoundly increased by geldanamycin (Figures 5B and 5C and Table S1). Four thousand four hundred six peaks of H3K9me3 were induced by geldanamycin but only one peak was found to be reduced ( $p < 0.05$ , fold change threshold  $\log_{2}FC = 0.5$ ). For H3K36me3, 1430 peaks were increased and only 213 peaks were decreased (Figure 5B). The impacted H3K9me3 peaks were mainly identified at promoters (35.6%), intergenic regions (20.7%), and introns (31.4%) (Figure 5D). The upregulated H3K36me3 peaks were mainly identified at intergenic regions (38%) and introns (54.3%), while the downregulated H3K36me3 peaks were predominantly at intron regions (77.4%) (Figure 5D). Gene set enrichment pathway analysis showed that the intergenic regions and introns with elevated H3K9me3 were significantly enriched with enhancers associated with *PAX3-FOXO1* binding sites (Figure 5E and Table S2), which was similar to the H3K36me3 that was increased at the intergenic and intron regions (Table S2). However, the promoters with increased H3K9me3



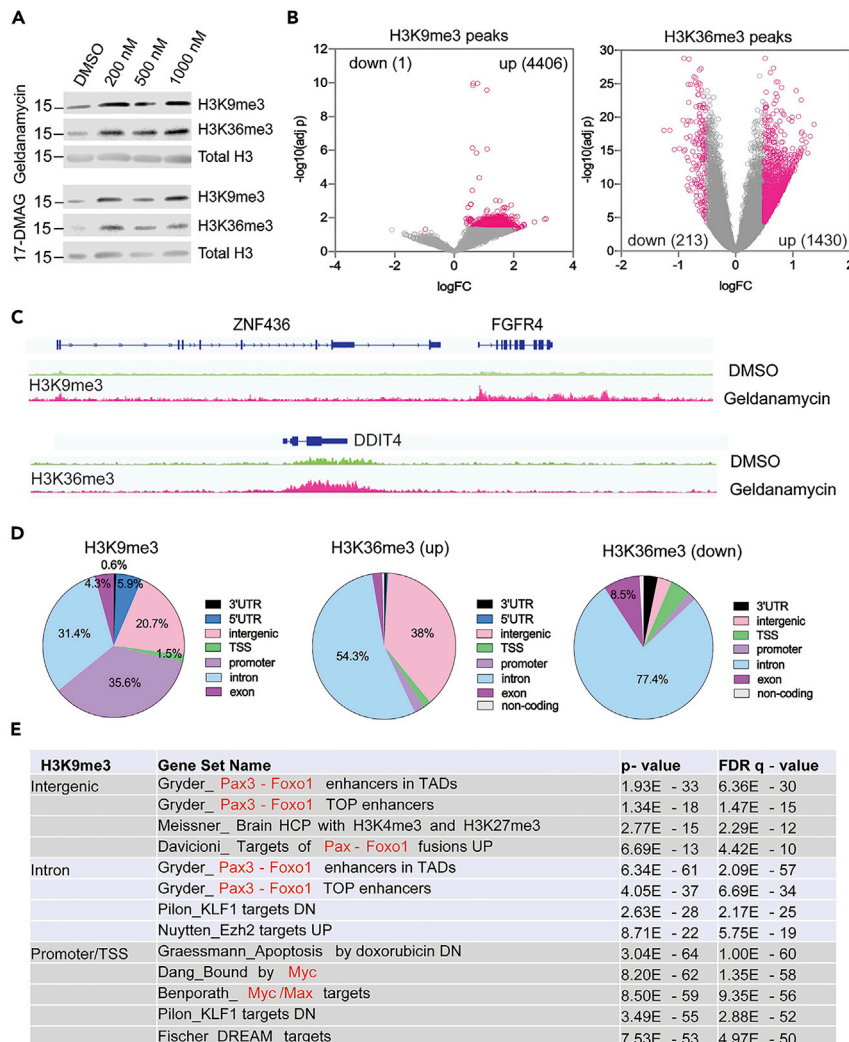


**Figure 5. Geldanamycin increases the KDM4B substrates H3K9me3 and H3K36me3 in aRMS cells.**

(A) Western blot assessment of H3K9me3 and H3K36me3 levels after Rh30 cells are treated with different concentrations of geldanamycin or 17-DMAG for 24 hr.

(B) Rh30 cells are treated with 1  $\mu$ M of geldanamycin for 24 hr and the H3K9me3 and H3K36me3 peaks across the genome are analyzed by ChIP-seq. Significant change is defined for each peak when  $p < 0.05$  and log fold change (LogFC) is no less than 0.5.

(C) The examples of H3K9me3 and H3K36me3 peaks at genomic loci of *FGFR4* and *DDIT4*, respectively, snapshot using IGV program. (D) The global distribution of H3K9me3 and H3K36me3 peaks at different regions of annotated genes.

3'UTR = 3' untranslated region, 5'UTR = 5' untranslated region, TSS = transcription start site.

(E) Gene set enrichment analysis defines the gene sets with elevated H3K9me3 peaks that are most significantly impacted by geldanamycin treatment, at different regions of the annotated genes.

See also [Tables S1](#) and [S2](#).

were enriched with Myc targets (Figure 5E). The genes associated with the downregulated H3K36me3 at introns were associated with cell cycle related transcription factor binding (Table S2). H3K9me3 is a heterochromatin mark, representing repressive gene transcription (Kouzarides, 2007). These data indicate that KDM inhibition by geldanamycin impacts the transcriptional activity of two oncogenic transcription factors, PAX3-FOXO1 and Myc. H3K36me3 is mainly enriched at gene bodies with active transcription (Kouzarides, 2007). The elevated H3K36me3 at intergenic regions and introns may disrupt active gene transcription. Thus, geldanamycin not only inhibits the enzymatic activity of KDM and increases the heterochromatic state of the PAX3-FOXO1 targets but also downregulates PAX3-FOXO1 oncoprotein levels by targeting Hsp90, thus making it a unique dual inhibitor.

### The geldanamycin analog 17-DMAG suppresses tumor growth and disrupts multiple oncogenic pathways and induces muscle differentiation signature

Previous studies reported that two specific and more potent Hsp90 inhibitors, AT13387 and Ganetespib, showed no effect on aRMS xenograft growth (Kang et al., 2012; Lock et al., 2013). Importantly, however, these two compounds did not inhibit KDM4B activity based on our assays (Figure S2). We hypothesized that geldanamycin and 17-DMAG might be more effective for PAX3-FOXO1-positive aRMS based on: (1) their ability to inhibit KDM activity and induction of heterochromatin marks of PAX3-FOXO1 and Myc targets; and (2) their ability to target PAX3-FOXO1 for proteasomal degradation. As geldanamycin has unfavorable pharmacokinetics *in vivo* and is associated with liver toxicity, we chose 17-DMAG and 17-AAG for *in vivo* assessment. After PAX3-FOXO1-positive Rh30 xenografts implanted in CB17 *scid* mice reached about 200 mm<sup>3</sup> in size, 17-DMAG or 17-AAG was given intraperitoneally at a dose of 25mg/kg or 50mg/kg, respectively, twice daily, every 4 days. 17-DMAG treatment significantly delayed tumor growth (Figure 6A) and extended mouse survival (Figure 6B). While 17-AAG has a more potent activity than 17-DMAG to inhibit Hsp90 (Asgharzadeh et al., 2006; Kamal et al., 2003), 17-AAG had only a very modest effect on tumor growth and survival (Figures 6A and 6B), which is consistent with its weaker potency in inhibiting KDM4B (Figure 3). These *in vivo* data were consistent with a previous study (Smith et al., 2008), which showed that 17-DMAG significantly inhibited tumor growth of aRMS. To understand how 17-DMAG affected PAX3-FOXO1-positive tumor growth, we performed RNA-seq to define the signaling pathways impacted by 17-DMAG in xenografts. RNA-seq analysis of the treated xenografts showed that PAX3-FOXO1 targets such as *FGFR4* and *MYCN* were significantly downregulated by 17-DMAG but not 17-AAG (Figure 6C and Table S3), in line with the combined effects of PAX3-FOXO1 degradation and the epigenetic impact on PAX3-FOXO1 target genes (Figures 4 and 5). Gene set enrichment analysis (GSEA) showed that 17-DMAG significantly inhibited MYC, E2F and NOTCH pathways (Ignatius et al., 2017; Slemmons et al., 2017; Takahashi et al., 2004; Tonelli et al., 2012) (Figure 6D), all of which are essential to cancer cell growth, proliferation and survival. Consistent with the *in vitro* results of differentiation marker induction by 17-DMAG (Figure S4), the muscle gene signature was significantly induced (Figure 6E), indicating that 17-DMAG induces aRMS cell differentiation in tumors. Immunohistochemical staining for the apoptosis marker Caspase 3 and a cell death marker TUNEL showed that 17-DMAG induced significant cancer cell death (Figures 6F and 6G). Taken together, 17-DMAG has potent antitumor effects and targets multiple oncogenic pathways in aRMS. Interestingly, a previous report showed that 17-DMAG was not effective against the PAX3-FOXO1-negative embryonal RMS (eRMS) (Smith et al., 2008), suggesting the specific activity of 17-DMAG against PAX3-FOXO1-positive tumors. Additionally, two specific and more potent Hsp90 inhibitors, AT13387 and Ganetespib, showed no effect on either aRMS or eRMS xenograft growth (Kang et al., 2012; Lock et al., 2013). This may be due to inability of these compounds to inhibit KDM, highlighting the importance of the KDM-inhibitory activity of 17-DMAG in treating aRMS.

### The anticancer activity of 17-DMAG is partly dependent on KDM4B

To test whether inhibition of KDM4B by 17-DMAG contributes to the anti-proliferative phenotype, we treated KDM4B-null Rh30 cells with 17-DMAG. Loss of KDM4B led to at least 3-fold greater resistance to 17-DMAG (Figures 7A–7C), suggesting that KDM4B, at least in part, is responsible for the anti-proliferative phenotype. Furthermore, we tested a selective KDM5 inhibitor KDM5-C70 (Tumber et al., 2017) and KDM6 inhibitor GSK-J4 (Kruidenier et al., 2012), both of which showed no anti-proliferative effect (Figures 7D and 7F) at the concentrations that hit the targets (Figures 7E and 7G). These data suggest that KDM4, but not other KDMs, are responsible for the anticancer activity of 17-DMAG.

### Combination of 17-DMAG with conventional chemotherapy enhances therapeutic efficacy

In addition to targeting the PAX3-FOXO1 pathway and other key oncogenic pathways (Figure 6), GSEA analysis revealed that 17-DMAG also inhibits gene signatures involved in DNA repair and the cell cycle (Figures S5A–S5D). We therefore surmised that 17-DMAG may enhance the efficacy of standard chemotherapy agents which damage DNA (such as irinotecan, a topoisomerase I inhibitor which generates DNA single- and double-strand breaks) and that halt the cell cycle (such as vincristine, an inhibitor of microtubule formation in mitotic spindle progression). The combination of vincristine and irinotecan (VCR + IRN) has been used in multiple clinical trials for relapsed patients with sarcoma (clinicaltrials.gov). We hypothesized that the combination of 17-DMAG and VCR + IRN may achieve better efficacy than either approach alone. Indeed, combining 17-DMAG significantly improved the efficacy of VCR + IRN in two PAX3-FOXO1-positive RMS xenograft models implanted in NSG mice (Figures 8A–8F). In the Rh30 xenograft model, all mice had a complete response (CR) to the combination therapy while nearly all control mice had progressive

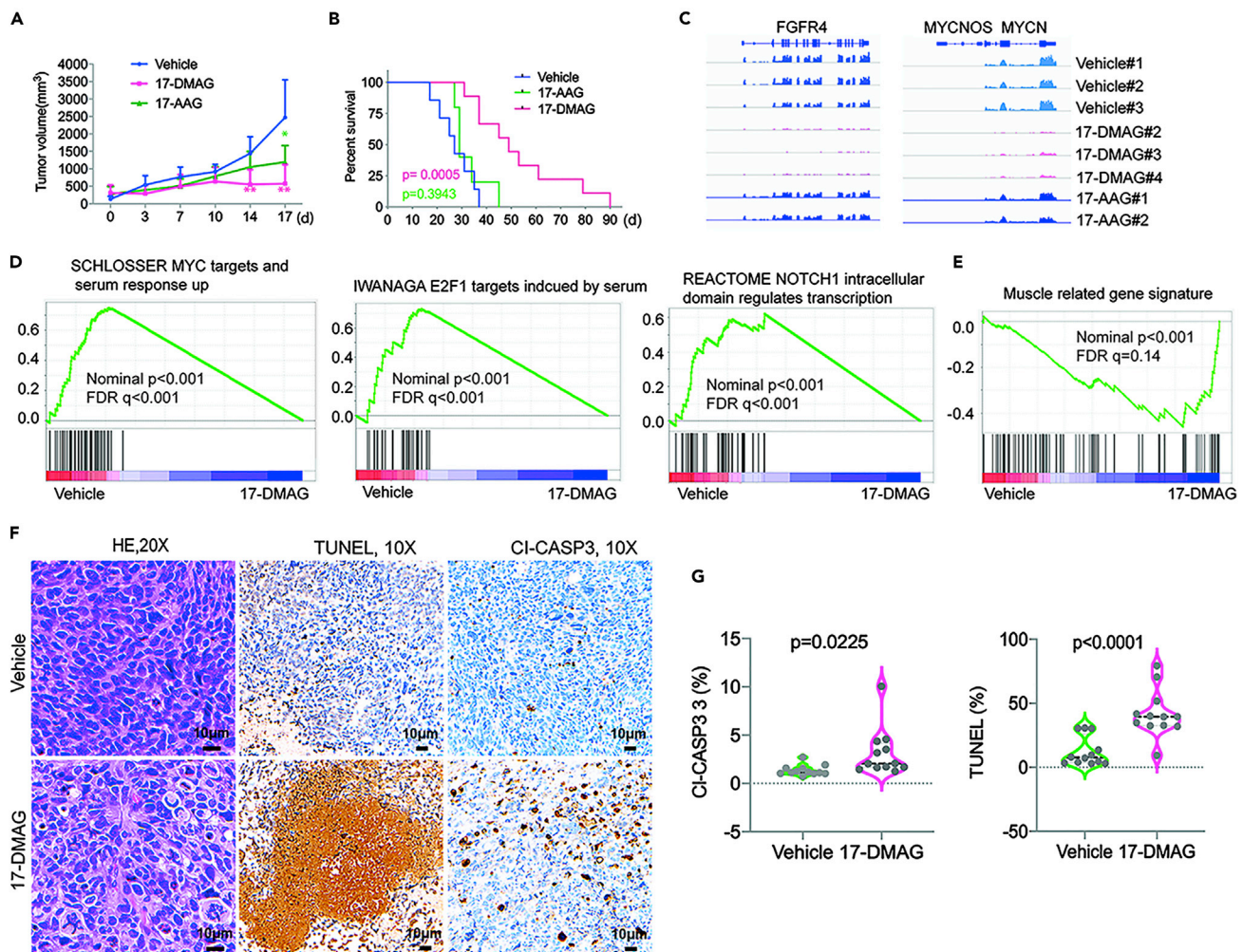


**Figure 6. 17-DMAG suppresses tumor growth, inhibits tumor angiogenesis, and disrupts multiple oncogenic pathways**

(A) Tumor growth curve of Rh30 in CB17 *scid* mice treated with vehicle (n = 7), 25mg/kg of 17-DMAG (n = 11) and 50mg/kg of 17-AAG (n = 7). Unpaired t test for comparison of tumor volumes of each group. \*\*p < 0.01, \*p < 0.05.

(B) Kaplan-Meier analysis of mouse survival treated with vehicle, 17-DMAG and 17-AAG. Log rank test for comparison of survival of each group. (C) RNA-seq read of *FGFR4* and *MYCN* from 3 individual tumors of vehicle, 3 individual tumors of 17-DMAG and 2 individual tumors of 17-AAG.

(D) GSEA analyses of pathways downregulated by 17-DMAG.

(E) GSEA analyses of pathways downregulated by 17-DMAG.

(F) Hematoxylin and Eosin (H&E), cleaved caspase 3 (CI-CASP3) and TUNEL immunohistochemistry staining of tumor tissue sections from vehicle and 17-DMAG treatment. (G) IHC scores of 3 different areas per section from 4 tumors (n = 12) in each group were compared with unpaired student t test. Data are represented as mean  $\pm$  SEM.

See also [Figures S4](#) and [S5](#) and [Table S3](#).

disease when treated with 17-DMAG alone or chemotherapy alone ([Figures 8A–8C](#)). In the Rh41 xenograft model, combination therapy also showed a better response (11% stable disease, 22% partial response, and 67% CR) than monotherapy ([Figures 7D](#) and [7F](#)).

## Discussion

Geldanamycin, and its analogs 17-AAG and 17-DMAG, are prototype Hsp90 inhibitors which bind the N-terminal pocket of Hsp90 ([Stebbins et al., 1997](#)), and have potent anticancer activity. However, the mechanism of action of these ansamycins is not entirely clear. It has been reported that geldanamycin and its analogs have inhibitory activity and binding affinity to Hsp90 in the range of 0.3–10  $\mu$ M ([Chiosis et al., 2001](#); [Panaretou et al., 1998](#); [Roe et al., 1999](#)), which is in contrast to the low nanomolar antiproliferative

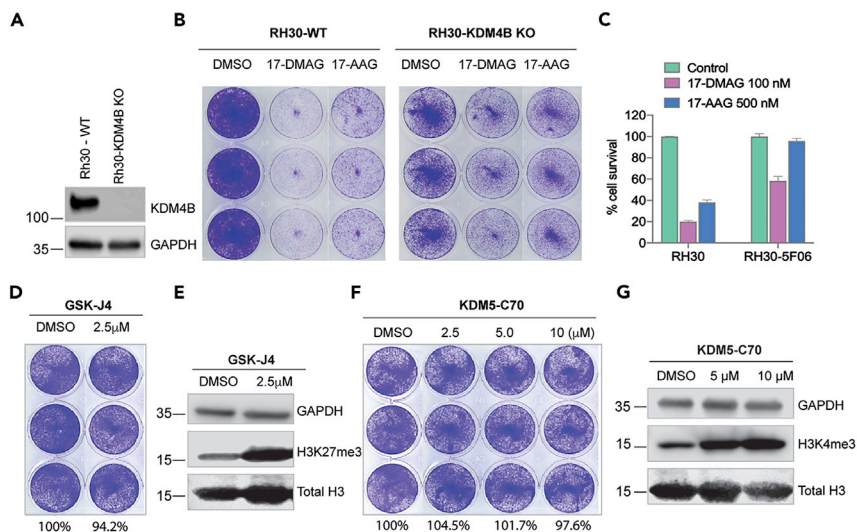


**Figure 7. The anticancer activity of 17-DMAG is partly dependent on KDM4B**

(A) Western blot shows KDM4B expression in Rh30 wildtype (Rh30-WT) and KDM4B knockout (Rh30-KDM4B KO) cells. (B) Rh30-WT and Rh30-KDM4B KO cells are treated with 100nM of 17-DMAG or 500nM of 17-AAG for 5 days, followed by crystal violet staining. (C) The intensity of cells stained by crystal violet in Figure 7B is quantified by ImageJ, which is then normalized to the DMSO control. (D) Rh30 cells are treated with 2.5μM of GSK-J4 for 5 days, followed by crystal violet staining. The values indicate the intensity of cells stained by crystal violet quantified by ImageJ, which is normalized to the DMSO control. (E) The whole cell lysates of Rh30 cells treated with GSK-J4 for 72 hr are assessed by Western blot with indicated antibodies. (F) Rh30 cells are treated with different concentrations of KDM5-C70 for 5 days, followed by crystal violet staining. The values indicate the intensity of cells stained by crystal violet quantified by ImageJ, which is normalized to the DMSO control. (G) The whole cell lysates of Rh30 cells treated with KDM5-C70 for 72 hr are assessed by Western blot with indicated antibodies.

activity of the compounds in multiple cell lines in culture (Chiosis et al., 2001; Neckers, 2002; Panaretou et al., 1998; Schulte and Neckers, 1998). Three major mechanisms were proposed to interpret the discrepancy of the 100-fold greater potency in cell culture. The first theory is ansamycins bind to and inhibit an Hsp90 multiprotein complex with much higher affinity than to Hsp90 alone (Kamal et al., 2003). The second explanation is that the physicochemical properties of the ansamycins result in greater intracellular accumulation from cell culture media (Chiosis et al., 2001), leading to highly potent antiproliferative activity. The third possible reason may be due to geldanamycin's time-dependent, tight binding to Hsp90 (Gooljarsingh et al., 2006). However, in this study, we identified geldanamycin and 17-DMAG as potent KDM inhibitors using multiple orthogonal validation approaches (TR-FRET, high-content immunofluorescence, MALDI-FTICR mass spectrometry, ALPHAscreen and MST assay), demonstrating that these compounds are epigenetic modulators. Other chemotypes of Hsp90 inhibitors showed no direct KDM inhibition, indicating that geldanamycin has unique features being a dual inhibitor of KDM/Hsp90.

Rhabdomyosarcoma (RMS) is a devastating myogenic cancer in children, adolescents, and young adults (Hettmer et al., 2014; Xia et al., 2002). This soft tissue sarcoma is mainly classified into two histological subtypes, aRMS and eRMS. aRMS is more aggressive, with a higher rate of metastasis and a poorer prognosis (Hettmer et al., 2014; Skapek et al., 2013; Sorensen et al., 2002). aRMS is primarily driven by the pathognomonic fusion oncoprotein PAX3-FOXO1 (Barr, 2001; Linardic, 2008) or its variant PAX7-FOXO1. However, no effective molecules are available to target PAX3-FOXO1 and its transcriptional activity. It was previously shown that 17-DMAG, the geldanamycin analog, was more potent at inhibiting the tumor growth of PAX3-FOXO1-positive aRMS but not PAX3-FOXO1-negative eRMS (Smith et al., 2008); while two other specific and more potent Hsp90 inhibitors, AT13387 and Ganetespib, showed no effect on either aRMS or eRMS xenograft growth (Kang et al., 2012; Lock et al., 2013). Our study provides evidence that the first prototype Hsp90 inhibitor geldanamycin and its analog 17-DMAG are new KDM inhibitors, exerting dual inhibition of

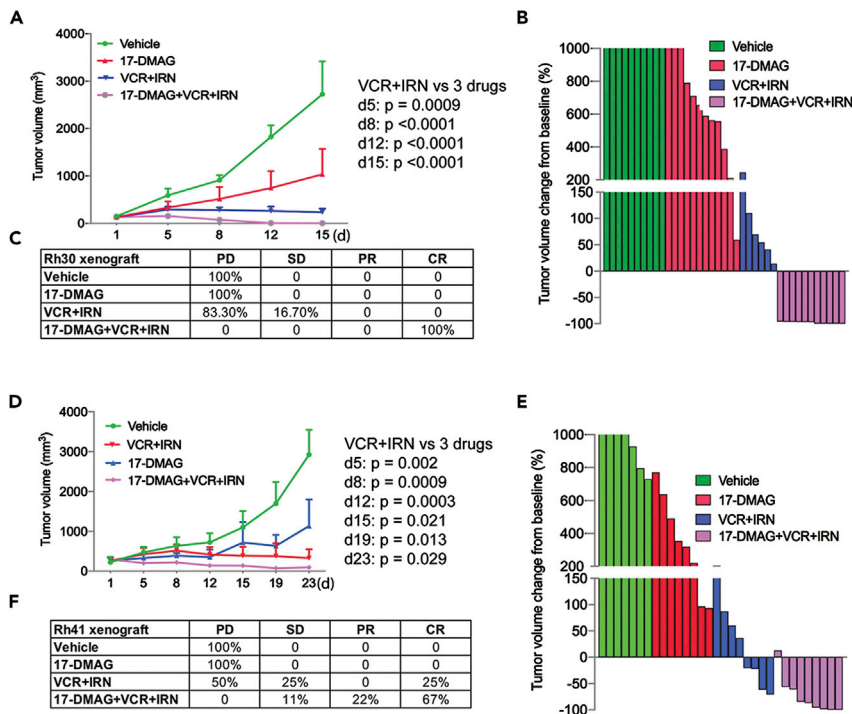


**Figure 8. Combination of 17-DMAG with conventional chemotherapy enhances therapeutic efficacy**

(A–C) Tumor growth curve of Rh30 in NSG mice treated with vehicle (n = 10), 17-DMAG (n = 12), VCR/IRN (n = 6), 17-DMAG/VCR/IRN (n = 11) for two weeks (A), Waterfall plot of response to treatment with 17-DMAG, VCR/IRN, and 17-DMAG/VCR/IRN (B), Summary of tumor response to treatment with 17-DMAG, VCR/IRN, and 17-DMAG/VCR/IRN (C). p value is determined by Wilcoxon Rank-Sum test between treatment groups VCR + IRN and 17-DMAG + VCR + IRN. (D–F) Tumor growth curve of Rh41 in NSG mice treated with vehicle (n = 7), 17-DMAG (n = 8), VCR + IRN (n = 8), 17-DMAG + VCR + IRN (n = 9) for three weeks (D), Waterfall plot of response to the treatment with 17-DMAG, VCR + IRN, and 17-DMAG + VCR + IRN (E), Summary of tumor response to the treatment with 17-DMAG, VCR/IRN, and 17-DMAG/VCR/IRN (F). p value is determined by Wilcoxon Rank-Sum test between treatment groups VCR + IRN and 17-DMAG + VCR + IRN.

Hsp90 and histone demethylases, which may account for the discrepancies of *in vivo* efficacy against aRMS among these Hsp90 inhibitors. 17-DMAG disrupted the epigenetic landscape of PAX3-FOXO1 target genes by elevating the histone marks H3K9me3 and H3K36me3 and inhibited the expression of PAX3-FOXO1 targets such as *FGFR4* and *MYCN*. Multiple oncogenic pathways including MYC, E2F1 and NOTCH were inhibited by 17-DMAG. Previous studies have shown that MYC, E2F1 and NOTCH pathways play an important role in RMS (Ignatius et al., 2017; Slemmons et al., 2017; Takahashi et al., 2004; Tonelli et al., 2012). Combination of 17-DMAG with conventional chemotherapy further enhanced efficacy. Our data provide a rationale for targeting PAX3-FOXO1-positive aRMS using chemotherapy in combination with KDM inhibitors. Nevertheless, other potential off-targeting molecules may also contribute to the therapeutic efficacy of 17-DMAG, as 17-AAG has been shown to bind to mitochondrial voltage-dependent anion channel and inhibits cell invasion (Xie et al., 2011), and ansamycins may also induce reactive oxygen species (Samuni et al., 2010). In the future, the optimization of 17-DMAG dosing in combination with chemotherapy might be key to find the optimal therapeutic window.

KDMs play an important role in carcinogenesis, metastasis and therapy resistance (D'Oto et al., 2016). Pharmacologically targeting KDM effectively inhibits tumor growth in multiple preclinical models (Grasso et al., 2015; Lochmann et al., 2018; Metzger et al., 2017; Pishas et al., 2018; Yang et al., 2017). KDM1 inhibitors have entered clinical trials in cancer treatment (Fang et al., 2019). We recently identified an antifungal drug ciclopirox as a JmjC-domain containing KDM inhibitor, which targets KDMs and suppresses neuroblastoma growth (Yang et al., 2017). Here, we further showed 17-DMAG inhibits RMS growth, providing a proof-of-concept that KDMs are a potential vulnerability of solid tumors driven by oncogenic transcription factors such as MYC and PAX3-FOXO1, whose activity may require epigenetic modifiers to facilitate their

transformation activity. Considering that most oncogenic transcription factors are difficult to target directly as they usually do not bear druggable pockets, targeting such epigenetic modifiers may provide alternative options to inhibiting cancer drivers. The surprising discovery of geldanamycin and its analogs as KDM inhibitors suggests that cancers driven by oncogenic transcription factors may be more sensitive to 17-DMAG than other chemotypes of Hsp90 inhibitor, considering that solid tumors are hypoxic and multiple KDMs are hypoxia-inducible genes (Yang et al., 2018). While the chaperone dependency of oncoproteins is already known, dependency of PAX3-FOXO1 on Hsp90 for protein stability has not been previously reported. Our study shows that PAX3-FOXO1 physically interacts with Hsp90 and pharmacologic inhibition of Hsp90 induces proteasome-dependent degradation of PAX3-FOXO1, indicating that PAX3-FOXO1 is a new Hsp90 client. This may further enhance the effect of geldanamycin/17-DMAG on PAX3-FOXO1 function, as the heterochromatin mark, H3K9m3 was profoundly elevated at PAX3-FOXO1 downstream target genes. As chimeric transcription factors such as MLL-AF9 and MOZ-TIF2 play a critical role in cellular transformation, and need KDM4 for their function<sup>26</sup> (Cheung et al., 2016), geldanamycin analogs might be suitable to target cancers driven by such oncofusion proteins, warranting further investigation using animal models.

Geldanamycin is a natural antibiotic isolated as the fermentation product of *Streptomyces hygroscopicus*, a bacterial strain widely distributed in nature, especially in the soil. Activity profiling of geldanamycin against KDMs showed that geldanamycin is more selective to inhibit human KDM4 and KDM5 members, two closest subfamilies in the KDM phylogenetic tree (Figure 3A). Why would a bacterium produce an antibiotic that is able to dually inhibit KDM and Hsp90? One possibility is that it may help bacteria more effectively defend surrounding competitors such as other bacterial strains or fungi. Although bacteria do not have homologs of KDM4 and KDM5, they do have JmjC domain containing proteins and Hsp90 homologs. However, based on phylogenetic analysis, fungi have homologs of KDM4 and KDM5 (Figure S6). 17-DMAG and 17-AAG, two derivatives of geldanamycin used in clinical application, have distinct selectivity against KDMs. While 17-DMAG showed a broader KDM inhibition to KDM3, KDM4, KDM5, and KDM6, 17-AAG seemed to be more selective to KDM4A and KDM4C. This might be the reason that 17-DMAG had a higher therapeutic efficacy than 17-AAG in suppressing tumor growth in aRMS xenograft models. Particularly, all three compounds showed very low activity to KDM1A ( $IC_{50} > 10\mu M$ ), which is not a JmjC domain containing demethylase. Notably, bacteria do not have KDM1 homologs (Zhou and Ma, 2008). These data indicate that geldanamycin has an evolutionary selectivity to JmjC KDMs. While the structural basis for selectivity of geldanamycin and its analogs against KDM remains to be solved, the selectivity is probably determined by the differences of 17-position of benzoquinone ring (17-methoxy group of geldanamycin, 17-dimethylaminoethylamino of 17-DMAG, and 17-N-allylamino of 17-AAG). Based on structural studies, this position is highly solvent-exposed in the Hsp90-Geldanamycin crystal complex and is a poor candidate for additional Hsp90 contacts (Stebbins et al., 1997), suggesting that it is not essential to Hsp90 binding. However, whether geldanamycin could inhibit other related dioxygenases such as TETs, PHDs, and ALKB whose activity also depend on  $Fe^{2+}$  and 2-oxoglutarate warrant further studies. Hsp90 has 3 families and warrants further studies to determine which one is important to RMS and whether depletion of Hsp90 could lead to same phenotype as KDM4B inhibition.

We noticed the  $IC_{50}$  values of geldanamycin were different among TR-FRET, HTRF, ALPHA screen, MALDI-FTICR and cell-based immunofluorescence assays. The TR-FRET  $IC_{50}$  value of 50.1 nM was only slightly different from the  $IC_{50}$  value of 84.4 nM observed in the HTRF assay. The TR-FRET assay and the HTRF assay were similarly formulated with slightly different acceptors (AF488-streptavidin in the TR-FRET assay vs AF647-streptavidin in the HTRF assay). The small difference in the acceptors was believed to contribute to the subtle  $IC_{50}$  value difference. While ALPHA assay is similar to TR-FRET, the KDM4B concentration and acceptor were different from our in-house TR-FRET, which may account for the  $IC_{50}$  difference. In the MALDI-FTICR assay, the substrate peptide concentration was 10  $\mu M$  instead of 1.5  $\mu M$  in the TR-FRET or HTRF, the higher concentration of the substrate peptide ultimately resulted an observed higher  $IC_{50}$  value of 1.24  $\mu M$ . In the cell-based immunofluorescence assay, an  $IC_{50}$  value of 21.2 nM for geldanamycin was observed which agreed well with the TR-FRET or HTRF assay, although protein binding, cellular permeability or metabolism may all complicate geldanamycin's cellular activity at different ways. Taken together, we believe different assay formats with different mechanisms contribute to the discrepancies of  $IC_{50}$ . Nevertheless, all these orthogonal methods validated geldanamycin as a KDM inhibitor.

In summary, we identified Hsp90 inhibitors, geldanamycin and its analog 17-DMAG, as potent KDM inhibitors. We also found that PAX3-FOXO1 is a Hsp90 client, which was destabilized by geldanamycin. Our

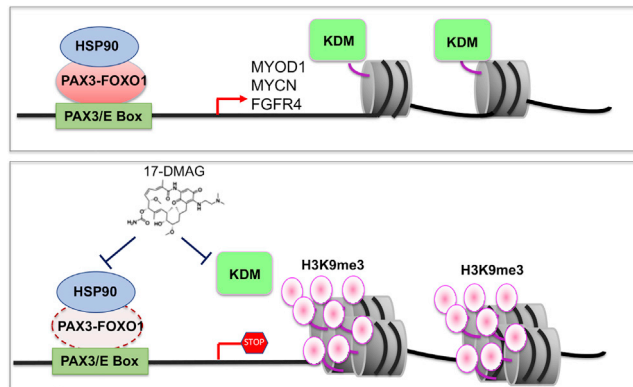


**Figure 9. Mechanism of action of geldanamycin or 17-DMAG**

PAX3-FOXO1 binds at enhancer regions enriched with PAX3 and E-box motifs (Cao et al., 2010), driving expression of the key oncogenes such as MYCN and FGFR4. KDM demethylates H3K9me3 at PAX3-FOXO1 target genes, maintaining the euchromatin status for facilitating active gene transcription mediated by PAX3-FOXO1. When targeted by 17-DMAG, KDM activity is inhibited, resulting in epigenetic reprogramming of PAX3-FOXO1 target genes by inducing heterochromatin mark H3K9me3, and consequently disrupting the transcriptional activity of PAX3-FOXO1. In addition, as an Hsp90 inhibitor, 17-DMAG leads to destabilization of the Hsp90 client PAX3-FOXO1, further enhancing the suppression of PAX3-FOXO1 function. Thus, being a dual KDM/Hsp90 inhibitor, 17-DMAG has more potent antitumor effects to PAX3-FOXO1-positive aRMS than other Hsp90 inhibitors.

findings support the concept that PAX3-FOXO1 creates an epigenetic dependency to KDMs and chaperone dependency to Hsp90, and thus dually targeting KDMs and Hsp90 is a potentially valuable therapeutic option for PAX3-FOXO1-driven aRMS (Figure 9).

### Limitations of the study

Our study has limitations in that geldanamycin/17-DMAG are not specific KDM4B inhibitors and further future experiments will be needed to clarify this and the mechanism of action.

### Resource availability

#### Lead contact

Further information and requests for resources and reagents should be directed to and will be fulfilled by the lead contact, Jun Yang (Jun.Yang2@stjude.org).

#### Materials availability

All unique/stable reagents generated in this study are available from the lead contact upon request pending completed Materials Transfer Agreement.

#### Data and code availability

The accession number for the RNA-seq and ChIP-seq data reported in this paper has been submitted to GEO, GSE151493 [ChIP-seq], GSE151514 [RNA-seq].

<https://www.ncbi.nlm.nih.gov/geo/query/acc.cgi?acc=GSE151598&token=utkpiockhrglnkx>

### Methods

All methods can be found in the accompanying [Transparent Methods supplemental file](#).

### Supplemental information

Supplemental information can be found online at <https://doi.org/10.1016/j.isci.2020.101996>.

## Acknowledgments

This work was partly supported by American Cancer Society-Research Scholar (130421-RSG-17-071-01-TBG, J.Y.) and National Cancer Institute (R03CA212802-01A1, J.Y.; 1R01CA229739-01, J.Y.). The content is solely the responsibility of the authors and does not necessarily represent the official views of the National Institutes of Health.

## Author contributions

A.A.Z., S.S., W.L., J.L., J.F., A.A., B.C., J.B., M.K.Y., A.A.T., D.F., J.M., H.T., B.Y., S.D., Q.W., and Z.L. performed research. A.A.Z., A.S., D.C., S.S., H.J., W.L., J.L., A.A., R.L., M.K.Y., J.Y. P.B., Z.L. analyzed data. J.Y., A.M.D. T.C., S.W., and Z.R. designed the research. J.Y. wrote the paper with input from A.M., C.T., A.M.D.

## Declaration of interests

The authors declare no competing interests.

Received: April 9, 2020

Revised: June 9, 2020

Accepted: December 23, 2020

Published: January 22, 2021

## References

- Ambati, S.R., Lopes, E.C., Kosugi, K., Mony, U., Zehir, A., Shah, S.K., Taldone, T., Moreira, A.L., Meyers, P.A., Chiosis, G., et al. (2014). Pre-clinical efficacy of PU-H71, a novel HSP90 inhibitor, alone and in combination with bortezomib in Ewing sarcoma. *Mol. Oncol.* 8, 323–336.
- Asgharzadeh, S., Pique-Regi, R., Sposto, R., Wang, H., Yang, Y., Shimada, H., Matthay, K., Buckley, J., Ortega, A., and Seeger, R.C. (2006). Prognostic significance of gene expression profiles of metastatic neuroblastomas lacking MYCN gene amplification. *J. Natl. Cancer Inst.* 98, 1193–1203.
- Barr, F.G. (2001). Gene fusions involving PAX and FOX family members in alveolar rhabdomyosarcoma. *Oncogene* 20, 5736–5746.
- Butler, L.M., Ferraldeschi, R., Armstrong, H.K., Centenera, M.M., and Workman, P. (2015). Maximizing the therapeutic potential of HSP90 inhibitors. *Mol. Cancer Res.* 13, 1445–1451.
- Cao, L., Yu, Y., Bilke, S., Walker, R.L., Mayeenuddin, L.H., Azorsa, D.O., Yang, F., Pineda, M., Helman, L.J., and Meltzer, P.S. (2010). Genome-wide identification of PAX3-FKHR binding sites in rhabdomyosarcoma reveals candidate target genes important for development and cancer. *Cancer Res.* 70, 6497–6508.
- Chen, J., Liu, H., Liu, J., Qi, J., Wei, B., Yang, J., Liang, H., Chen, Y., Chen, J., Wu, Y., et al. (2013). H3K9 methylation is a barrier during somatic cell reprogramming into iPSCs. *Nat. Genet.* 45, 34–42.
- Chen, Y.K., Bonaldi, T., Cuomo, A., Del Rosario, J.R., Hosfield, D.J., Kanouni, T., Kao, S.C., Lai, C., Lobo, N.A., Matuszkiewicz, J., et al. (2017). Design of KDM4 inhibitors with antiproliferative effects in cancer models. *ACS Med. Chem. Lett.* 8, 869–874.
- Cheng, Y., Yuan, Q., Vergnes, L., Rong, X., Youn, J.Y., Li, J., Yu, Y., Liu, W., Cai, H., Lin, J.D., et al. (2018). KDM4B protects against obesity and metabolic dysfunction. *Proc. Natl. Acad. Sci. U S A* 115, E5566–E5575.
- Cheung, N., Fung, T.K., Zeisig, B.B., Holmes, K., Rane, J.K., Mowen, K.A., Finn, M.G., Lenhard, B., Chan, L.C., and So, C.W. (2016). Targeting aberrant epigenetic networks mediated by PRMT1 and KDM4C in acute myeloid leukemia. *Cancer Cell* 29, 32–48.
- Chi, P., Allis, C.D., and Wang, G.G. (2010). Covalent histone modifications—miswritten, misinterpreted and mis-erased in human cancers. *Nat. Rev. Cancer* 10, 457–469.
- Chiosis, G., Rosen, N., and Sepp-Lorenzino, L. (2001). LY294002-geldanamycin heterodimers as selective inhibitors of the PI3K and PI3K-related family. *Bioorg. Med. Chem. Lett.* 11, 909–913.
- Chu, C.H., Wang, L.Y., Hsu, K.C., Chen, C.C., Cheng, H.H., Wang, S.M., Wu, C.M., Chen, T.J., Li, L.T., Liu, R., et al. (2014). KDM4B as a target for prostate cancer: structural analysis and selective inhibition by a novel inhibitor. *J. Med. Chem.* 57, 5975–5985.
- Coffey, K., Rogerson, L., Ryan-Munden, C., Alkharaf, D., Stockley, J., Heer, R., Sahadevan, K., O'Neill, D., Jones, D., Darby, S., et al. (2013). The lysine demethylase, KDM4B, is a key molecule in androgen receptor signalling and turnover. *Nucleic Acids Res.* 41, 4433–4446.
- D'Oto, A., Tian, Q.W., Davidoff, A.M., and Yang, J. (2016). Histone demethylases and their roles in cancer epigenetics. *J. Med. Oncol. Ther.* 1, 34–40.
- Das, P.P., Shao, Z., Beyaz, S., Apostolou, E., Pinello, L., Angeles, A.L., O'Brien, K., Atsma, J.M., Fujiwara, Y., Nguyen, M., et al. (2014). Distinct and combinatorial functions of Jmjd2b/Kdm4b and Jmjd2c/Kdm4c in mouse embryonic stem cell identity. *Mol. Cell* 53, 32–48.
- Duan, L., Chen, Z., Lu, J., Liang, Y., Wang, M., Roggero, C.M., Zhang, Q.J., Gao, J., Fang, Y., Cao, J., et al. (2019). Histone lysine demethylase KDM4B regulates the alternative splicing of the androgen receptor in response to androgen deprivation. *Nucleic Acids Res.* 47, 11623–11636.
- Duan, L., Rai, G., Roggero, C., Zhang, Q.J., Wei, Q., Ma, S.H., Zhou, Y., Santoyo, J., Martinez, E.D., Xiao, G., et al. (2015). KDM4/JMJD2 histone demethylase inhibitors block prostate tumor growth by suppressing the expression of AR and MYB-regulated genes. *Chem. Biol.* 22, 1185–1196.
- Esteller, M. (2008). Epigenetics in cancer. *N. Engl. J. Med.* 358, 1148–1159.
- Fang, Y., Liao, G., and Yu, B. (2019). LSD1/KDM1A inhibitors in clinical trials: advances and prospects. *J. Hematol. Oncol.* 12, 129.
- Gooljarsingh, L.T., Fernandes, C., Yan, K., Zhang, H., Grooms, M., Johanson, K., Sinnamon, R.H., Kirkpatrick, R.B., Kerrigan, J., Lewis, T., et al. (2006). A biochemical rationale for the anticancer effects of Hsp90 inhibitors: slow, tight binding inhibition by geldanamycin and its analogues. *Proc. Natl. Acad. Sci. U S A* 103, 7625–7630.
- Grasso, C.S., Tang, Y., Truffaux, N., Berlow, N.E., Liu, L., Debily, M.A., Quist, M.J., Davis, L.E., Huang, E.C., Woo, P.J., et al. (2015). Functionally defined therapeutic targets in diffuse intrinsic pontine glioma. *Nat. Med.* 21, 827.
- Greer, E.L., and Shi, Y. (2012). Histone methylation: a dynamic mark in health, disease and inheritance. *Nat. Rev. Genet.* 13, 343–357.
- Gryder, B.E., Yohe, M.E., Chou, H.C., Zhang, X., Marques, J., Wachtel, M., Schaefer, B., Sen, N., Song, Y., Gualtieri, A., et al. (2017). PAX3-FOXO1 establishes myogenic super enhancers and confers BET bromodomain vulnerability. *Cancer Discov.* 7, 884–899.



- Guo, J., Dai, X., Laurent, B., Zheng, N., Gan, W., Zhang, J., Guo, A., Yuan, M., Liu, P., Asara, J.M., et al. (2019). AKT methylation by SETDB1 promotes AKT kinase activity and oncogenic functions. *Nat. Cell Biol* 21, 226–237.
- Hahm, E.R., Moura, M.B., Kelley, E.E., Van Houten, B., Shiva, S., and Singh, S.V. (2011). Withaferin A-induced apoptosis in human breast cancer cells is mediated by reactive oxygen species. *PLoS One* 6, e23354.
- Hettmer, S., Li, Z., Billin, A.N., Barr, F.G., Cornelison, D.D., Ehrlich, A.R., Guttridge, D.C., Hayes-Jordan, A., Helman, L.J., Houghton, P.J., et al. (2014). Rhabdomyosarcoma: current challenges and their implications for developing therapies. *Cold Spring Harb Perspect. Med.* 4, a025650.
- Hillringhaus, L., Yue, W.W., Rose, N.R., Ng, S.S., Gileadi, C., Loenarz, C., Bello, S.H., Bray, J.E., Schofield, C.J., and Oppermann, U. (2011). Structural and evolutionary basis for the dual substrate selectivity of human KDM4 histone demethylase family. *J. Biol. Chem.* 286, 41616–41625.
- Højfeldt, J.W., Agger, K., and Helin, K. (2013). Histone lysine demethylases as targets for anticancer therapy. *Nat. Rev. Drug Discov.* 12, 917–930.
- Huether, R., Dong, L., Chen, X., Wu, G., Parker, M., Wei, L., Ma, J., Edmonson, M.N., Hedlund, E.K., Rusch, M.C., et al. (2014). The landscape of somatic mutations in epigenetic regulators across 1,000 paediatric cancer genomes. *Nat. Commun.* 5, 3630.
- Ignatius, M.S., Hayes, M.N., Lobbardi, R., Chen, E.Y., McCarthy, K.M., Sreenivas, P., Motala, Z., Durbin, A.D., Molodtsov, A., Reeder, S., et al. (2017). The NOTCH1/SNAIL1/MEF2C pathway regulates growth and self-renewal in embryonal rhabdomyosarcoma. *Cell Rep* 19, 2304–2318.
- Jez, J.M., Chen, J.C., Rastelli, G., Stroud, R.M., and Santi, D.V. (2003). Crystal structure and molecular modeling of 17-DMAG in complex with human Hsp90. *Chem. Biol.* 10, 361–368.
- Kamal, A., Thao, L., Sensintaffar, J., Zhang, L., Boehm, M.F., Fritz, L.C., and Burrows, F.J. (2003). A high-affinity conformation of Hsp90 confers tumour selectivity on Hsp90 inhibitors. *Nature* 425, 407–410.
- Kandath, C., McLellan, M.D., Vandin, F., Ye, K., Niu, B., Lu, C., Xie, M., Zhang, Q., McMichael, J.F., Wyczalkowski, M.A., et al. (2013). Mutational landscape and significance across 12 major cancer types. *Nature* 502, 333–339.
- Kang, M.H., Reynolds, C.P., Houghton, P.J., Alexander, D., Morton, C.L., Kolb, E.A., Gorlick, R., Keir, S.T., Carol, H., Lock, R., et al. (2012). Initial testing (Stage 1) of AT13387, an HSP90 inhibitor, by the pediatric preclinical testing program. *Pediatr. Blood Cancer* 59, 185–188.
- Kawazu, M., Saso, K., Tong, K.I., McQuire, T., Goto, K., Son, D.O., Wakeham, A., Miyagishi, M., Mak, T.W., and Okada, H. (2011). Histone demethylase JMJD2B functions as a co-factor of estrogen receptor in breast cancer proliferation and mammary gland development. *PLoS One* 6, e17830.
- King, O.N., Li, X.S., Sakurai, M., Kawamura, A., Rose, N.R., Ng, S.S., Quinn, A.M., Rai, G., Mott, B.T., Beswick, P., et al. (2010). Quantitative high-throughput screening identifies 8-hydroxyquinolines as cell-active histone demethylase inhibitors. *PLoS One* 5, e15535.
- Kooistra, S.M., and Helin, K. (2012). Molecular mechanisms and potential functions of histone demethylases. *Nat. Rev. Mol. Cell Biol* 13, 297–311.
- Kouzarides, T. (2007). Chromatin modifications and their function. *Cell* 128, 693–705.
- Kruidenier, L., Chung, C.W., Cheng, Z., Liddle, J., Che, K., Joberty, G., Bantscheff, M., Bountra, C., Bridges, A., Diallo, H., et al. (2012). A selective jumoni H3K27 demethylase inhibitor modulates the proinflammatory macrophage response. *Nature* 488, 404–408.
- Linardic, C.M. (2008). PAX3-FOXO1 fusion gene in rhabdomyosarcoma. *Cancer Lett.* 270, 10–18.
- Lochmann, T.L., Powell, K.M., Ham, J., Floros, K.V., Heisey, D.A.R., Kurupi, R.I.J., Calbert, M.L., Ghotra, M.S., Greninger, P., Dozmorov, M., et al. (2018). Targeted inhibition of histone H3K27 demethylation is effective in high-risk neuroblastoma. *Sci. Transl. Med.* 10, ea04680.
- Lock, R.B., Carol, H., Maris, J.M., Kang, M.H., Reynolds, C.P., Kolb, E.A., Gorlick, R., Keir, S.T., Billups, C.A., Kurmasheva, R.T., et al. (2013). Initial testing (stage 1) of ganetespib, an Hsp90 inhibitor, by the pediatric preclinical testing program. *Pediatr. Blood Cancer* 60, E42–E45.
- Martin, C., and Zhang, Y. (2005). The diverse functions of histone lysine methylation. *Nat. Rev. Mol. Cell Biol* 6, 838–849.
- Metzger, E., Stepputtis, S.S., Strietz, J., Preca, B.T., Urban, S., Willmann, D., Allen, A., Zenk, F., Iovino, N., Bronsert, P., et al. (2017). KDM4 inhibition targets breast cancer stem-like cells. *Cancer Res.* 77, 5900–5912.
- Mishra, S., Van Rechem, C., Pal, S., Clarke, T.L., Chakraborty, D., Mahan, S.D., Black, J.C., Murphy, S.E., Lawrence, M.S., Daniels, D.L., et al. (2018). Cross-talk between lysine-modifying enzymes controls site-specific DNA amplifications. *Cell* 175, 1716.
- Neckers, L. (2002). Heat shock protein 90 inhibition by 17-allylamino-17-demethoxygeldanamycin: a novel therapeutic approach for treating hormone-refractory prostate cancer. *Clin. Cancer Res.* 8, 962–966.
- Panaretou, B., Prodromou, C., Roe, S.M., O'Brien, R., Ladbury, J.E., Piper, P.W., and Pearl, L.H. (1998). ATP binding and hydrolysis are essential to the function of the Hsp90 molecular chaperone in vivo. *EMBO J.* 17, 4829–4836.
- Peng, C., Brain, J., Hu, Y., Goodrich, A., Kong, L., Grayzel, D., Pak, R., Read, M., and Li, S. (2007). Inhibition of heat shock protein 90 prolongs survival of mice with BCR-ABL-T3151-induced leukemia and suppresses leukemic stem cells. *Blood* 110, 678–685.
- Pishas, K.I., Drenberg, C.D., Taslim, C., Theisen, E.R., Johnson, K.M., Saund, R.S., Pop, I.L., Crompton, B.D., Lawlor, E.R., Tirode, F., et al. (2018). Therapeutic targeting of KDM1A/LSD1 in ewing sarcoma with SP-2509 engages the endoplasmic reticulum stress response. *Mol. Cancer Ther.* 17, 1902–1916.
- Richards, M.W., Law, E.W., Rennalls, L.P., Busacca, S., O'Regan, L., Fry, A.M., Fennell, D.A., and Bayliss, R. (2014). Crystal structure of EML1 reveals the basis for Hsp90 dependence of oncogenic EML4-ALK by disruption of an atypical beta-propeller domain. *Proc. Natl. Acad. Sci. U S A* 111, 5195–5200.
- Rodriguez-Paredes, M., and Esteller, M. (2011). Cancer epigenetics reaches mainstream oncology. *Nat. Med.* 17, 330–339.
- Roe, S.M., Prodromou, C., O'Brien, R., Ladbury, J.E., Piper, P.W., and Pearl, L.H. (1999). Structural basis for inhibition of the Hsp90 molecular chaperone by the antitumor antibiotics radicicol and geldanamycin. *J. Med. Chem.* 42, 260–266.
- Samuni, Y., Ishii, H., Hyodo, F., Samuni, U., Krishna, M.C., Goldstein, S., and Mitchell, J.B. (2010). Reactive oxygen species mediate hepatotoxicity induced by the Hsp90 inhibitor geldanamycin and its analogs. *Free Radic. Biol. Med.* 48, 1559–1563.
- Schulte, T.W., and Neckers, L.M. (1998). The benzoquinone ansamycin 17-allylamino-17-demethoxygeldanamycin binds to HSP90 and shares important biologic activities with geldanamycin. *Cancer Chemother. Pharmacol.* 42, 273–279.
- Seidel, S.A., Dijkman, P.M., Lea, W.A., van den Bogaart, G., Jerabek-Willemsen, M., Lazić, A., Joseph, J.S., Srinivasan, P., Baaske, P., Simeonov, A., et al. (2013). Microscale thermophoresis quantifies biomolecular interactions under previously challenging conditions. *Methods* 59, 301–315.
- Seoane, J.A., Kirkland, J.G., Caswell-Jin, J.L., Crabtree, G.R., and Curtis, C. (2019). Chromatin regulators mediate anthracycline sensitivity in breast cancer. *Nat. Med.* 25, 1721–1727.
- Shi, Y. (2007). Histone lysine demethylases: emerging roles in development, physiology and disease. *Nat. Rev. Genet.* 8, 829–833.
- Shi, Y., Lan, F., Matson, C., Mulligan, P., Whetstone, J.R., Cole, P.A., Casero, R.A., and Shi, Y. (2004). Histone demethylation mediated by the nuclear amine oxidase homolog LSD1. *Cell* 119, 941–953.
- Shi, Y., and Whetstone, J.R. (2007). Dynamic regulation of histone lysine methylation by demethylases. *Mol. Cell* 25, 1–14.
- Skapek, S.X., Anderson, J., Barr, F.G., Bridge, J.A., Gastier-Foster, J.M., Parham, D.M., Rudzinski, E.R., Triche, T., and Hawkins, D.S. (2013). PAX-FOXO1 fusion status drives unfavorable outcome for children with rhabdomyosarcoma: a children's oncology group report. *Pediatr. Blood Cancer* 60, 1411–1417.
- Slemmons, K.K., Crose, L.E.S., Riedel, S., Sushnitha, M., Belyea, B., and Linardic, C.M. (2017). A novel notch-YAP circuit drives stemness and tumorigenesis in embryonal rhabdomyosarcoma. *Mol. Cancer Res.* 15, 1777–1791.

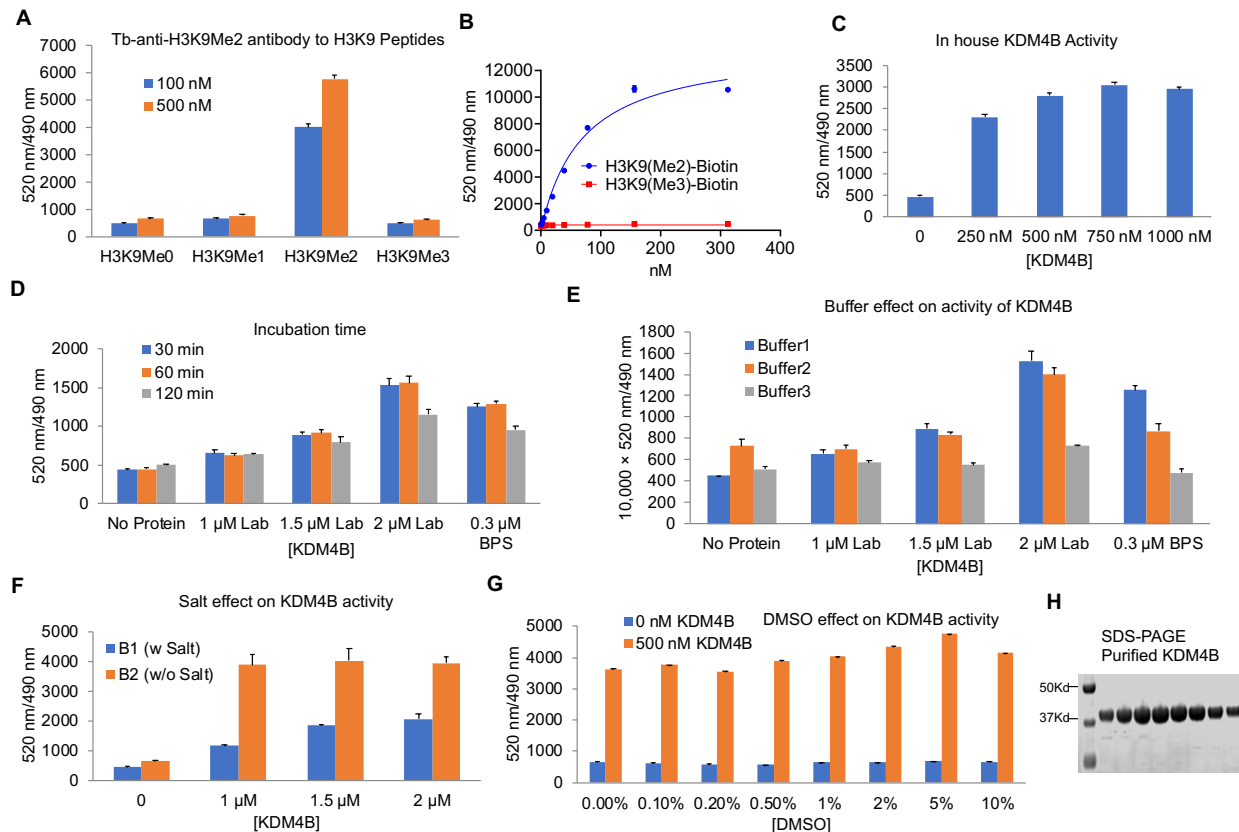
- Smith, M.A., Morton, C.L., Phelps, D.A., Kolb, E.A., Lock, R., Carol, H., Reynolds, C.P., Maris, J.M., Keir, S.T., Wu, J., et al. (2008). Stage 1 testing and pharmacodynamic evaluation of the HSP90 inhibitor alvespimycin (17-DMAG, KOS-1022) by the pediatric preclinical testing program. *Pediatr. Blood Cancer* *51*, 34–41.
- Sorensen, P.H., Lynch, J.C., Qualman, S.J., Tirabosco, R., Lim, J.F., Maurer, H.M., Bridge, J.A., Crist, W.M., Triche, T.J., and Barr, F.G. (2002). PAX3-FKHR and PAX7-FKHR gene fusions are prognostic indicators in alveolar rhabdomyosarcoma: a report from the children's oncology group. *J. Clin. Oncol.* *20*, 2672–2679.
- Stebbins, C.E., Russo, A.A., Schneider, C., Rosen, N., Hartl, F.U., and Pavletich, N.P. (1997). Crystal structure of an Hsp90-geldanamycin complex: targeting of a protein chaperone by an antitumor agent. *Cell* *89*, 239–250.
- Takahashi, Y., Oda, Y., Kawaguchi, K., Tamiya, S., Yamamoto, H., Suita, S., and Tsuneyoshi, M. (2004). Altered expression and molecular abnormalities of cell-cycle-regulatory proteins in rhabdomyosarcoma. *Mod. Pathol.* *17*, 660–669.
- Tonelli, R., McIntyre, A., Camerin, C., Walters, Z.S., Di Leo, K., Selfe, J., Purgato, S., Missiaglia, E., Tortori, A., Renshaw, J., et al. (2012). Antitumor activity of sustained N-myc reduction in rhabdomyosarcomas and transcriptional block by antineoplastic therapy. *Clin. Cancer Res.* *18*, 796–807.
- Tumber, A., Nuzzi, A., Hookway, E.S., Hatch, S.B., Velupillai, S., Johansson, C., Kawamura, A., Savitsky, P., Yapp, C., Szykowska, A., et al. (2017). Potent and selective KDM5 inhibitor stops cellular demethylation of H3K4me3 at transcription start sites and proliferation of MM1S myeloma cells. *Cell Chem Biol* *24*, 371–380.
- Wang, W., Oguz, G., Lee, P.L., Bao, Y., Wang, P., Terp, M.G., Ditzel, H.J., and Yu, Q. (2018). KDM4B-regulated unfolded protein response as a therapeutic vulnerability in PTEN-deficient breast cancer. *J. Exp. Med.* *215*, 2833–2849.
- Whitesell, L., Mimnaugh, E.G., De Costa, B., Myers, C.E., and Neckers, L.M. (1994). Inhibition of heat shock protein HSP90-pp60v-src heteroprotein complex formation by benzoquinone ansamycins: essential role for stress proteins in oncogenic transformation. *Proc. Natl. Acad. Sci. U S A* *91*, 8324–8328.
- Wilson, C., and Krieg, A.J. (2019). KDM4B: a nail for every hammer? *Genes (Basel)* *10*, 134.
- Xia, S.J., Pressey, J.G., and Barr, F.G. (2002). Molecular pathogenesis of rhabdomyosarcoma. *Cancer Biol. Ther.* *1*, 97–104.
- Xie, Q., Wondergem, R., Shen, Y., Cavey, G., Ke, J., Thompson, R., Bradley, R., Daugherty-Holtrop, J., Xu, Y., Chen, E., et al. (2011). Benzoquinone ansamycin 17AAG binds to mitochondrial voltage-dependent anion channel and inhibits cell invasion. *Proc. Natl. Acad. Sci. U S A* *108*, 4105–4110.
- Yang, J., Altahan, A.M., Hu, D., Wang, Y., Cheng, P.H., Morton, C.L., Qu, C., Nathwani, A.C., Shohet, J.M., Fotsis, T., et al. (2015). The role of histone demethylase KDM4B in Myc signaling in neuroblastoma. *J. Natl. Cancer Inst.* *107*, djv080.
- Yang, J., Harris, A.L., and Davidoff, A.M. (2018). Hypoxia and hormone-mediated pathways converge at the histone demethylase KDM4B in cancer. *Int. J. Mol. Sci.* *19*, 240.
- Yang, J., Jubb, A.M., Pike, L., Buffa, F.M., Turley, H., Baban, D., Leek, R., Gatter, K.C., Ragoussis, J., and Harris, A.L. (2010). The histone demethylase JMJD2B is regulated by estrogen receptor alpha and hypoxia, and is a key mediator of estrogen induced growth. *Cancer Res.* *70*, 6456–6466.
- Yang, J., Ledaki, I., Turley, H., Gatter, K.C., Montero, J.C., Li, J.L., and Harris, A.L. (2009). Role of hypoxia-inducible factors in epigenetic regulation via histone demethylases. *Ann. N. Y. Acad. Sci.* *1177*, 185–197.
- Yang, J., Milasta, S., Hu, D., Altahan, A.M., Interiano, R.B., Zhou, J., Davidson, J., Low, J., Lin, W., Bao, J., et al. (2017). Targeting histone demethylases in MYC-driven neuroblastomas with cyclopirox. *Cancer Res.* *77*, 4626–4638.
- Ye, L., Fan, Z., Yu, B., Chang, J., Al Hezaimi, K., Zhou, X., Park, N.H., and Wang, C.Y. (2012). Histone demethylases KDM4B and KDM6B promotes osteogenic differentiation of human MSCs. *Cell Stem Cell* *11*, 50–61.
- Young, L.C., McDonald, D.W., and Hendzel, M.J. (2013). Kdm4b histone demethylase is a DNA damage response protein and confers a survival advantage following gamma-irradiation. *J. Biol. Chem.* *288*, 21376–21388.
- Zhang, J.H., Chung, T.D., and Oldenburg, K.R. (1999). A simple statistical parameter for use in evaluation and validation of high throughput screening assays. *J. Biomol. Screen* *4*, 67–73.
- Zhou, X., and Ma, H. (2008). Evolutionary history of histone demethylase families: distinct evolutionary patterns suggest functional divergence. *BMC Evol. Biol.* *8*, 294.

## **Supplemental Information**

### **17-DMAG dually inhibits Hsp90 and histone lysine demethylases in alveolar rhabdomyosarcoma**

**Shivendra Singh, Ahmed Abu-Zaid, Wenwei Lin, Jonathan Low, Alireza Abdolvahabi, Hongjian Jin, Qiong Wu, Bailey Cooke, Jie Fang, John Bowling, Sivaraja Vaithiyalingam, Duane Currier, Mi-Kyung Yun, Dinesh M. Fernando, Julie Maier, Heather Tillman, Purva Bulsara, Zhaohua Lu, Sourav Das, Anang Shelat, Zhenmei Li, Brandon Young, Richard Lee, Zoran Rankovic, Andrew J. Murphy, Stephen W. White, Andrew M. Davidoff, Taosheng Chen, and Jun Yang**

## Supplemental Information



### Supplementary Figure 1. Optimization of the TR-FRET assay. Related to Figure 1.

(A) The Tb-anti-H3K9me2 antibody is very specific to the Biotin-H3K9Me2 peptide. Specificity test of the Tb-anti-H3K9me2 antibody against Biotin-H3K9me0, Biotin-H3K9me1, Biotin-H3K9me2, or Biotin H3K9me3 at 100 nM and 500 nM, respectively. (B) The Tb-anti-H3K9Me2 antibody is very specific to the product peptide Biotin-H3K9me2 (Blue curve), but not to the substrate peptide Biotin H3K9me3 (Red curve) at a wide concentration range tested. (C) The in-house KDM4B activity tested with the TR-FRET assay at selected concentrations of 0 nM, 250 nM, 500 nM, 750 nM and 1000 nM. (D) The effect of various incubation times on KDM4B activity in the TR-FRET assay. No KDM4B protein group (Background group), lab produced KDM4B protein at 1  $\mu$ M (1  $\mu$ M Lab), 1.5  $\mu$ M (1.5  $\mu$ M Lab), 2  $\mu$ M (2  $\mu$ M Lab), or BPS Bioscience KDM4B protein at 0.3  $\mu$ M ((0.3  $\mu$ M BPS) was tested for comparison. (E) The effect of 3 representative buffers on KDM4B activity in the TR-FRET assay. No KDM4B protein group (Background group), lab produced KDM4B protein at 1  $\mu$ M (1  $\mu$ M Lab), 1.5  $\mu$ M (1.5  $\mu$ M Lab), 2  $\mu$ M (2  $\mu$ M Lab), or BPS Bioscience KDM4B protein at 0.3  $\mu$ M ((0.3  $\mu$ M BPS) was tested for comparison. Buffer 1: 50 mM Tris-HCl (pH 8.0), 50 mM KCl, 10 mM MgCl<sub>2</sub>, 1 mM  $\alpha$ -ketoglutarate, 80  $\mu$ M FeSO<sub>4</sub>, 2 mM ascorbic acid, 0.01% BSA.

Buffer 2: 50 mM HEPES (pH 7.5), 1 mM  $\alpha$ -ketoglutarate, 2 mM L-ascorbic acid, 50  $\mu$ M FeSO<sub>4</sub>, 0.01% BSA.

Buffer 3: 50 mM HEPES (pH 7.5), 50 mM KCl, 10 mM MgCl<sub>2</sub>, 1 mM  $\alpha$ -ketoglutarate, 2 mM L-ascorbic acid, 50  $\mu$ M FeSO<sub>4</sub>, 0.01% BSA.

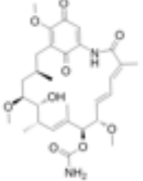
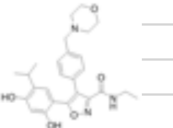
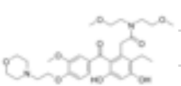
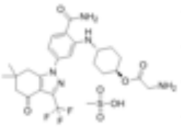
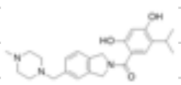
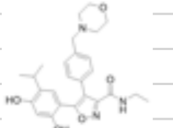
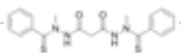
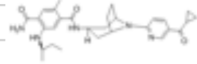
**(F)** The effect of salt on KDM4B activity in the TR-FRET assay. No KDM4B protein group (Background group), lab produced KDM4B protein at 1  $\mu$ M, 1.5  $\mu$ M, or 2  $\mu$ M was tested under indicated buffer condition for comparison.

B1 (w Salt): 50 mM Tris-HCl (pH 8.0), 50 mM KCl, 10 mM MgCl<sub>2</sub>, 1 mM  $\alpha$ -ketoglutarate, 80  $\mu$ M FeSO<sub>4</sub>, 2 mM ascorbic acid, 0.01% BSA

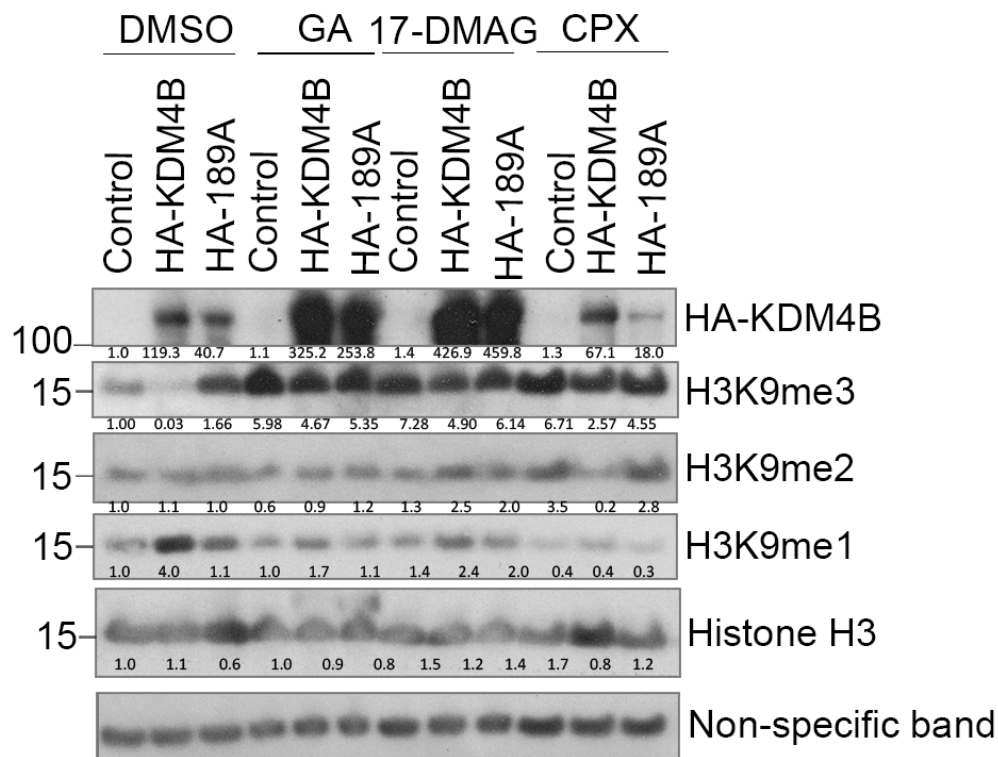
B2 (w/o Salt): 50 mM Tris-HCl (pH 8.0), 1 mM  $\alpha$ -ketoglutarate, 80  $\mu$ M FeSO<sub>4</sub>, 2 mM ascorbic acid, 0.01% BSA

**(G)** The effect of DMSO on KDM4B activity in the TR-FRET assay. No KDM4B protein group (Background group) or lab produced KDM4B protein at 500 nM was tested for comparison at indicated DMSO concentration.

**(H)** High purity and active catalytic domain of KDM4B that is expressed and purified from bacteria. Photo was taken after SDS-PAGE following Coomassie Blue R-250 Staining.

HSP90i	Company	Structure	TR-FRET activity (@15μM)
Geldanamycin			90%
Ganetespib	Synta Pharmaceuticals		12%
KW2478	Kyowa Hakko Kirin		4%
SNX-5422	Serenex/Pfizer		3%
AT13387	Astex		2%
NVP-AUY922	Novartis		-7%
STA-4783	Synta Pharmaceuticals		-7%
XL888	Daiichi Sankyo Inc		-107%

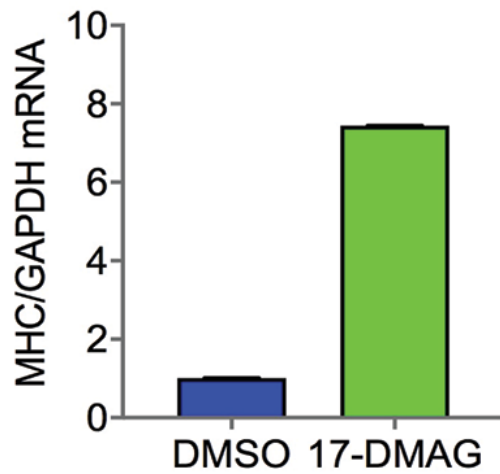
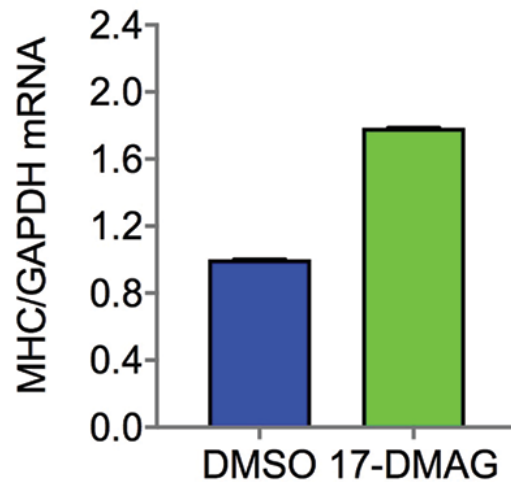
**Supplementary Figure 2. KDM4B inhibiting activity of different chemotypes of HSP90 inhibitors assessed by the TR-FRET assay. Related to Figure 1.**



**Supplementary Figure 3. Geldanamycin and 17-DMAG inhibit KDM4B enzymatic activity in cells. Related to Figure 2.**

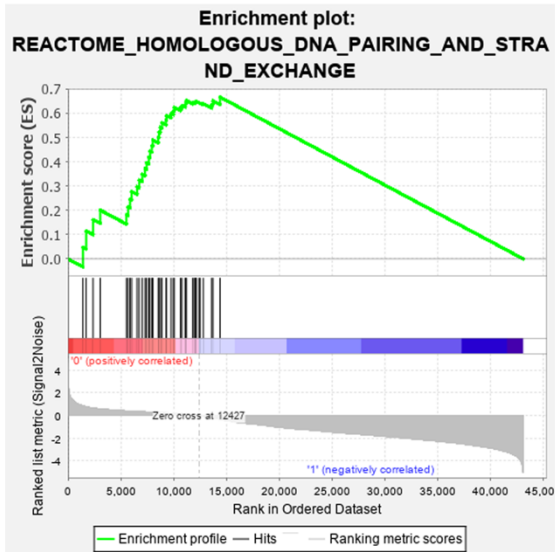
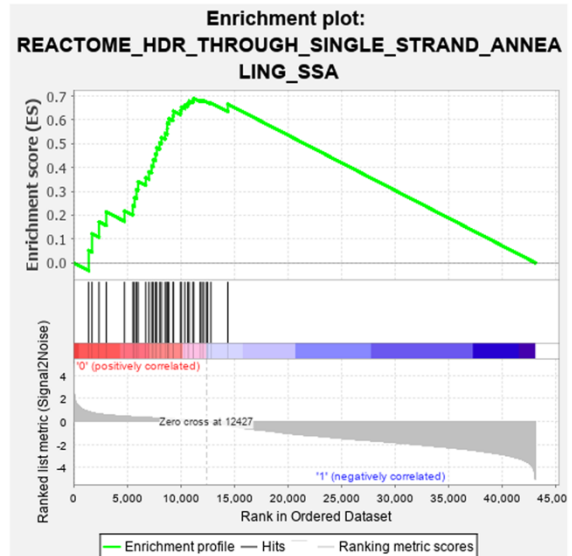
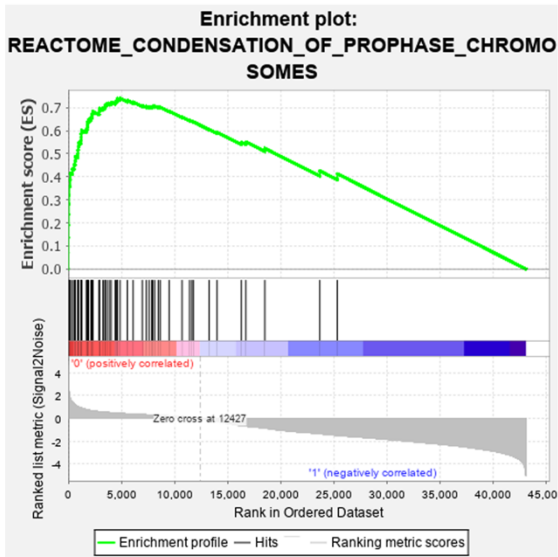
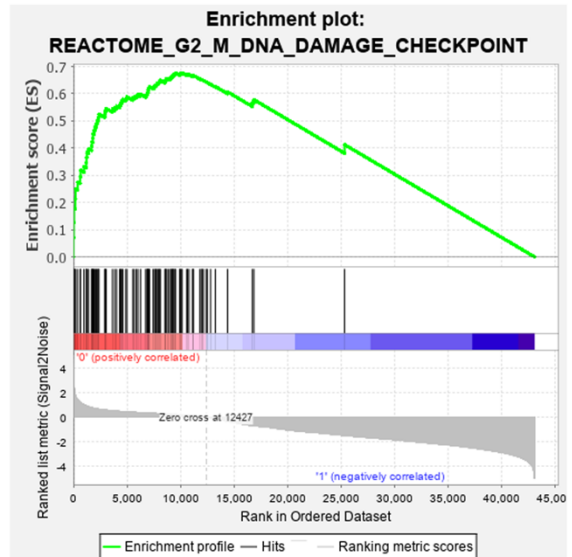
293T cells were transiently transfected with pCMV-HA-KDM4B and pCMV-HA-KDM4B(H189A). Eight hours later following transfection, cells were treated with 1  $\mu$ M of geldanamycin, 1  $\mu$ M of 17-DMAG and 5  $\mu$ M of ciclopirox (CPX) for 24 hours. Whole cell lysates were harvested for western blotting with indicated antibodies.



**A****B**

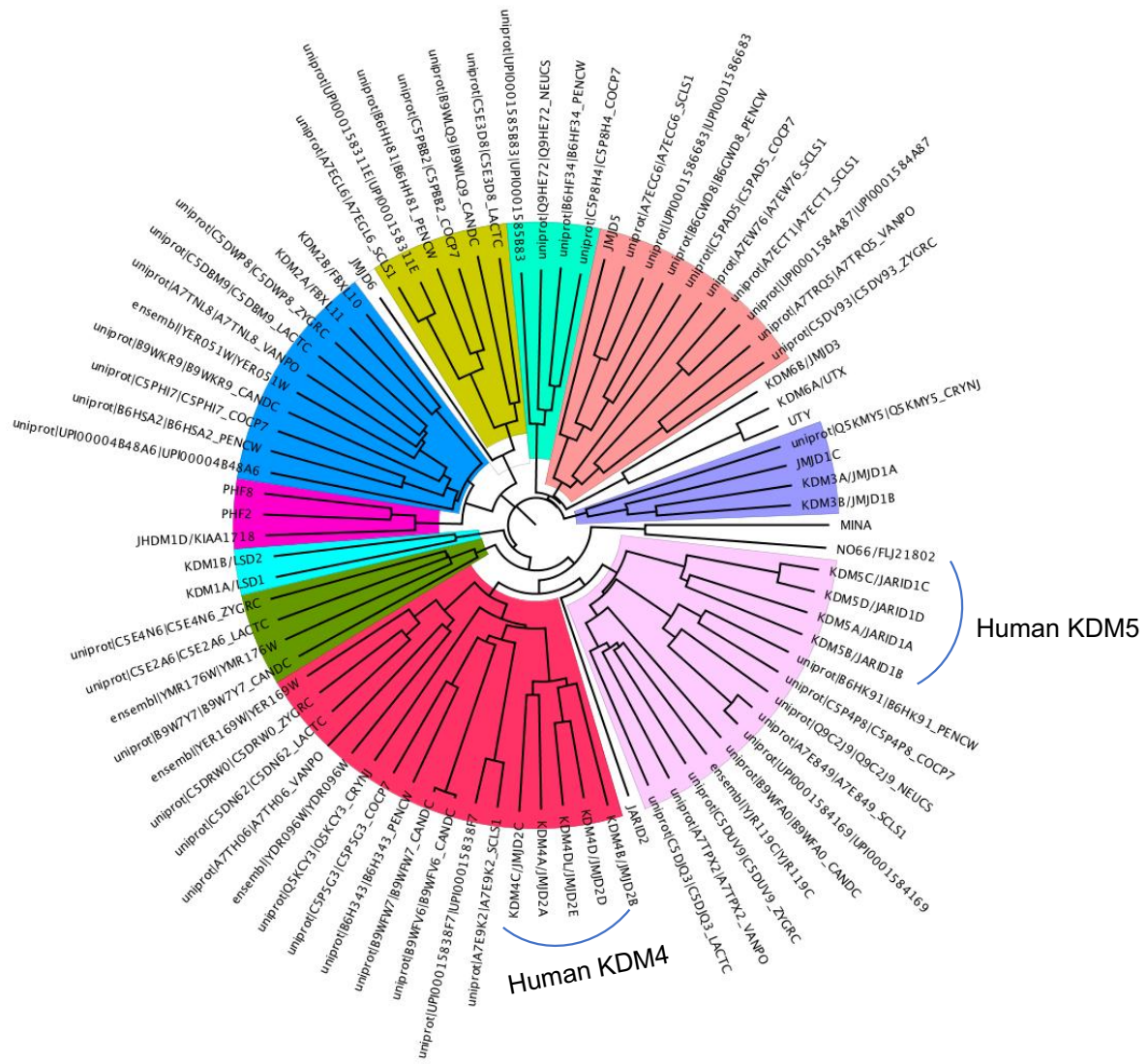
**Supplementary Figure 4. 17-DMAG induces RMS cell differentiation. Related to Figure 6.**

Induction of differentiation marker, muscle heavy chain (*MHC*) by 17-DMAG.  $10^5$  of Rh30 (A) or Rh41 (B) cells were seeded in a 6-well plate in 2 ml of complete RPMI medium. 24h later, 17-DMAG was added to a final concentration of 200nM, for 72h incubation. RNA was extracted and cDNA was synthesized. Quantitative PCR was performed to assess the differentiation marker gene *MHC* and the control *GAPDH* for normalization. The experiment was performed in biological triplicates. Data are represented as mean +/- SEM.

**A****B****C****D**

**Supplementary Figure 5. 17-DMAG inhibits the gene signatures of DNA repair and cell cycle. Related to Figure 6.**

GSEA analysis reveals that 17-DMAG downregulates the genes involved in homologous DNA pairing and strand exchange (**A**), homologous DNA repairing through single strand annealing (**B**), condensation of prophase chromosomes (**C**), and G2/M phase DNA damage checkpoint (**D**).



**Supplementary Figure 6. Phylogenetic tree of JmjC domains of KDM in human and fungus. Related to Figure 9.**

## TRANSPARENT METHODS

### Cell lines and reagents

*Cell lines* 293T, U2OS, Rh30, Rh41 cell lines were purchased from ATCC and validated by short tandem repeat (STR) using Promega PowerPlex 16 HS System once per month. PCR-based method was used for detection of Mycoplasma with LookOut Mycoplasma PCR Detection Kit (Sigma) and JumpStart *Taq* DNA Polymerase (Sigma) once per month to ensure cells were mycoplasma negative.

*Compounds.* 17-DMAG, 17-AAG, geldanamycin, AT13387, Ganetespib, GSK-J4 were purchased from Selleckchem. 17-AG was purchased from Santa Cruz Biotechnology. MG132 and Cyclopirox were purchased from Sigma. Vincristine, Irinotecan were purchased from MedChem Express (MCE). KDM5-C70 was purchased from Xcessbio.

*Antibodies.* The anti-PAX3-FOXO1 mouse monoclonal antibody was provided by Dr. Liang Cao (NCI). The anti-KDM4B antibody (A301-478A) was purchased from Bethyl Laboratories. The anti-Actin antibody (A2228) was purchased from Sigma. Anti-H3K4me3 (07-473) and Anti-normal mouse IgG antibody (12-371) was purchased from Millipore. The anti-total H3 (4499), anti-H3K9me3 (13969), anti-H3K36me3 (9763), anti-H3K4me3 (9751), H3K27me3 (9733) antibodies were purchased from Cell Signaling Technology (CST). Anti-FOXO1 antibody (2880) that recognizes the fusion protein PAX3-FOXO1 was purchased from CST. Anti-Hsp90 antibody (F-8) (sc-13119), anti-Hsp70 antibody (C92F3A-5)(sc-66048) and p53 antibody (DO-1) were purchased from Santa Cruz Biotechnology. Secondary horseradish peroxidase(HRP)-conjugated goat anti-mouse (31430) and goat anti-rabbit (31460) antibodies were purchased from Thermo Fisher Scientific.

*Plasmids.* MSCV-KDM4B(wt)-RFP and MSCV-KDM4B(H189A)-RFP constructs were generated by PCR of the full length of wild type and mutant KDM4B following by subcloning into MSCV-IRES-RFP plasmid, and standard retroviral packaging. U2OS cells were transduced with retroviral particles for high-content image screen. pCMV-HA-KDM4B was obtained from Addgene (24181). The catalytic domain of KDM4B(1-348) was subcloned into pET28a to produce histidine tagged KDM4B protein by Protein Production Facility at St Jude for TR-FRET and MALDI-FTICR screening.

### TR-FRET demethylation functional assay

Stock compound solutions (10 mM compound in DMSO) or DMSO only (vehicle control) were transferred to the individual wells in low volume black 384-well assay plates containing 1.5  $\mu$ M

biotin-H3K9me3 in 10  $\mu$ L assay buffer [50 mM Tris-HCl (pH 8.0), 1 mM  $\alpha$ -ketoglutarate, 80  $\mu$ M FeSO<sub>4</sub>, 2 mM ascorbic acid, 0.01% BSA] by using a V&P 384-well pintool (V&P Scientific, San Diego, CA) at 30 nL/well. KDM4B protein (750 nM) or buffer only was then dispensed (5  $\mu$ L/well). After a brief spin down and shake, the plates were incubated at room temperature for 30 min. Detection reagent (5  $\mu$ L/well) of 8 nM Tb-anti-H3K9me2 antibody and 8 nM AF488-streptavidin was dispensed, followed by a brief spin down, shake and 15 min room temperature incubation. The TR-FRET signal (fluorescence emission ratio of 10,000  $\times$  520 nm/490 nm) from each well was collected with a PHERAstar FS plate reader (BMG LABTECH Inc., Cary, NC). The final tested compound concentration was 20  $\mu$ M and the final DMSO concentration was 0.2% for all wells in the primary screening. The DMSO control wells with KDM4B protein and those without KDM4B protein were used as negative (0% inhibition) and positive (100% inhibition) controls, respectively. The individual compound activities were normalized to those of negative and positive controls. Compounds with %Inhibition  $\geq$  30% were selected as hits for DR analysis (10 concentrations, following a 1:3 serial dilution scheme; final concentration range 4.7 nM to 93.3  $\mu$ M, in triplicates) under similar assay condition as the primary screening, with the exception of the final DMSO concentration at 0.93% for all assay wells. The activity data for individual chemicals were normalized to that of positive and negative controls and fit into sigmoidal DR equation, if applicable, to derive DR curves and IC<sub>50</sub> values with GraphPad Prism 8.0.

### **High-content immunofluorescence imaging assay**

1000 U2OS-KDM4B expressing cells in 25  $\mu$ L of media were plated into each well of a poly-D-lysine coated Perkin Elmer 384-well View plates (Perkin Elmer 6007710) with a Thermo Scientific Wellmate. The cells were then grown for 18 hours overnight before they were drugged using a VP scientific pintool with S100 pins. The cells were then treated with compound for a twenty-four hours. Following treatment, the cells were fixed with 4% formaldehyde for 20 minutes at 37°C and permeabilized with 0.1% Triton-X 100 for 15 minutes at 25°C. Fixative was removed and each well washed with PBS. Cells were blocked using 1% BSA in PBS for 1 hour at 25°C. The primary antibody against trimethyl-histone H3 at Lys9 (Millipore 07-442) was used at 1/400 dilution in 1% BSA in PBS. This mixture was added to each well before incubation overnight at 4°C. Each well was then washed 3 times with PBS using a Biotek plate washer, and incubated for 1 hour at 25°C with a solution containing 1/400 goat  $\alpha$ -rabbit-Alexa-488 (Cell Signaling 4412S) and 1  $\mu$ M Hoechst 34580 to detect nuclear material (H21486 Molecular Probes.) Two images were captured of each well at 10X using a GE Healthcare InCell 6000 at 405 to detect nuclear staining and 488 nm to detect H3K9me3. The number of nuclear objects in each well, as detected through Hoechst

staining, was compared to the number of cells in each well expressing a minimum amount of H3K9me3 as determined by Alexa-488 fluorescence (1.5 million counts total intensity), to identify the percentage of cells in each considered “H3K9me3 Positive.” Averages shown are the result of eight replicate measurements per data point.

#### **Dose response HTRF demethylation functional assay**

Those selected hits with %Inhibition  $\geq$  30% from the TR-FRET demethylation functional assay were subjected to a HTRF demethylation functional assay with condition similar to the TR-FRET assay, except that the AF488-streptavidin was replaced with AF647-strepavidin. For data normalization, the DMSO control wells with KDM4B protein and those without KDM4B protein were defined as negative (0% inhibition) and positive (100% inhibition) controls, respectively. The individual compound activities were normalized to that of negative and positive controls and fit into sigmoidal DR equation, if applicable, to derive DR curves and IC<sub>50</sub> values with GraphPad Prism 8.0.

#### **MALDI-FTICR mass spectrometry-based demethylation assay**

To assess the inhibition potency of geldanamycin and its analogs, we used a MALDI-TOF MS-based platform developed by our group. A truncated version of KDM4B that contains only the JmjC catalytic domain, KDM4B(1-348) was used. KDM4B(1-348), to a final concentration of 250 nM (in 50 mM Tris base, pH 7.3), was incubated with different concentrations of each compound (10 concentrations in total) for 1 hour at room temperature. The final concentration of DMSO in each well was 1 %. As negative control, KDM4B(1-348) was incubated with 1 % DMSO. Positive control wells contained 10 % formic acid. Reactions were initiated upon adding the “substrate mixture” (200  $\mu$ M  $\alpha$ -ketoglutarate, 100  $\mu$ M ascorbate, 10  $\mu$ M NH<sub>4</sub>Fe(SO<sub>4</sub>)<sub>2</sub>, and 10  $\mu$ M H3K9me3(1-15) peptide) to each well. Reactions were incubated for 90 min at room temperature (to achieve ~ 20 % Turnover) prior to quenching with 10 % formic acid. Assays were performed in triplicates (n = 3).

Two microliters from each well were mixed with 18  $\mu$ L of MALDI matrix solution (20 mg/mL of 2,5 dihydroxybenzoic acid dissolved in 95 % methanol), from which 1  $\mu$ L was spotted on a 384 AnchorChip® MALDI target plate. Crystallized samples were then analyzed using a 7 T Solarix XR Fourier Transform Ion Cyclotron Resonance (FT-ICR) mass spectrometer (Bruker Co., MA, USA). The MALDI-FTICR parameters were optimized as follows: laser power = 20 % at 200 shots, laser shot frequency = 800 Hz, isolated Q1 m/z = 1530  $\pm$  20. The mass of two species were

detected:  $m/z = 1530.87$  (substrate), and  $m/z = 1516.85$  (dimethylated product). The following

formula was used to calculate % Turnover: 
$$\% \text{ Turnover} = \left( \frac{I_P}{I_P + I_S} \right) \times 100$$

Where  $I_P$  and  $I_S$  are the ion intensities of product and substrate, respectively. Values for % Turnover were then normalized based on negative and positive controls.

### **ALPHA Screen demethylation assay**

All reagents including KDM proteins were provided by BPS Bioscience company. All of the enzymatic reactions were conducted in duplicate at room temperature for 60 minutes in a 10  $\mu$ l mixture containing assay buffer, histone H3 peptide substrate, demethylase enzyme, and the test compounds. These 10  $\mu$ l reactions were carried out in wells of 384-well Optiplate (PerkinElmer). The dilution of the compounds was first performed in 100% DMSO with the highest concentration at 0.5mM. Each intermediate compound dilution (in 100% DMSO) will then get directly diluted 30x fold into assay buffer for 3.3x conc (DMSO). Enzyme only and blank only wells have a final DMSO concentration of 1%. From this intermediate step, 3  $\mu$ l of compound is added to 4  $\mu$ l of demethylase enzyme dilution is incubated for 30 minutes at room temperature. After this incubation, 3  $\mu$ l of peptide substrate is added. The final DMSO concentration is 1%. After enzymatic reactions, 5  $\mu$ l of anti-Mouse Acceptor beads (PerkinElmer, diluted 1:500 with 1x detection buffer) or 5  $\mu$ l of anti-Rabbit Acceptor beads (PerkinElmer, diluted 1:500 with 1x detection buffer) and 5  $\mu$ l of Primary antibody (BPS, diluted 1:200 with 1x detection buffer) were added to the reaction mix. After brief shaking, plate was incubated for 30 minutes. Finally, 10  $\mu$ l of AlphaScreen Streptavidin-conjugated donor beads (Perkin, diluted 1:125 with 1x detection buffer) were added. In 30 minutes, the samples were measured in AlphaScreen microplate reader (EnSpire Alpha 2390 Multilabel Reader, PerkinElmer). Enzyme activity assays were performed in duplicates at each concentration. The A-screen intensity data were analyzed and compared. In the absence of the compound, the intensity ( $C_e$ ) in each data set was defined as 100% activity. In the absence of enzyme, the intensity ( $C_0$ ) in each data set was defined as 0% activity. The percent activity in the presence of each compound was calculated according to the following equation:  $\% \text{ activity} = (C - C_0) / (C_e - C_0)$ , where  $C$  = the A-screen intensity in the presence of the compound.

The values of % activity versus a series of compound concentrations were plotted using non-linear regression analysis of Sigmoidal dose-response curve generated with the equation  $Y = B + (T - B) / (1 + 10^{((\text{LogEC}_{50} - X) \times \text{Hill Slope}))}$ , where  $Y$  = percent activity,  $B$  = minimum percent activity,  $T$  = maximum percent activity,  $X$  = logarithm of compound and Hill Slope = slope factor or

Hill coefficient. The IC<sub>50</sub> value was determined by the concentration causing a half-maximal percent activity.

### **Microscale Thermophoresis assay**

KDM4B was labeled with a cysteine reactive fluorescent dye (Protein Labeling Kit RED-MALEIMIDE, Nanotemper GmbH). A serial dilution of titrant was prepared in MST buffer containing 10 mM HEPES (pH 7.5), 200 mM NaCl, 2 mM NiCl<sub>2</sub>, 5% DMSO and 0.05% Tween 20. An equal volume of diluted titrant and the constant concentration of labeled KDM4B were added and loaded in a standard treated capillaries (Nanotemper GmbH). Binding measurements were performed on a Monolith NT.115 Blue/Red instrument (Nanotemper GmbH) at 40 % LED power and 40 % MST power. The data were analyzed using MO Affinity Analysis software (Nanotemper GmbH).

### **Phylogenetic tree analysis**

Amino acid sequences of KDM domains of histone lysine demethylases were aligned with Clustal Omega program (<https://www.ebi.ac.uk/Tools/msa/clustalo/>) and the phylogenetic tree was generated using neighbor-joining method, which was shown using iTOL program (<https://itol.embl.de>).

### **RNA-seq**

Total RNA was extracted from xenograft tissues by RNeasy Mini Kit (cat. # 74104) from QIAGEN. Paired-end sequencing was performed using the High-Seq platform with 100bp read length. Reads were aligned to the human GRCh37-lite using SJCRH's Strongarm pipeline. Counts per gene were obtained using htseq-count version 0.6.1 with Gencode vM5 level 1 and 2 gene annotations. Counts were normalized with VOOM and analyzed with LIMMA within the R statistical environment. Significance was defined as having a false discovery rate (FDR) <0.05. VOOM normalized counts were analyzed with Gene Set Enrichment Analysis (GSEA)<sup>79</sup>.

### **RNA-extraction and RT PCR**

The RNA extraction and RT PCR were performed as we previously described. Briefly, RNA was extracted using the RNeasy Mini Kit from Qiagen according to the manul. cDNA was synthesized using SuperScript™ II (Thermo Fisher). RT-PCR was performed using an Applied Biosystems 7500 Real-Time PCR system. The results were analyzed using  $\Delta\Delta$ CT methods. Fold-differences calculated using the  $\Delta\Delta$ CT method are expressed as a range by incorporating the standard deviation of the  $\Delta\Delta$ CT value into the fold- difference calculation according to the manufacture's



PCR Guide instructions (Applied Biosystem). The PCR primer sequences for  $\alpha$ -actin (forward primer 5-CCAACCGCGAGAAGATGA-3; reverse primer 5-CCAGAGGCGTACAGGGATAG-3), Muscle heavy chain (MHC) gene (forward primer 5-TCCTGGATGCCAGTGAGC-3; reverse primer 5-CCAGCTTCTTCTTGGTGTGA-3), Pax3-Foxo1 (forward primer CATGGATTTTCCAGCTATACAGAC; reverse primer 5-GTTCCTTCATTCTGCACACG-3), GAPDH (forward primer 5-AACGGGAAGCTTGTCATCAATGGAAA-3; Reverse primer 5-GCATCAGCAGAGGGGGCAGAG-3).

### **Western blot**

Cells were washed twice with ice-cold phosphate-buffered saline (PBS) and then directly lysed on ice with 2X sample loading buffer (0.1 M Tris HCl [pH 6.8], 200 mM dithiothreitol [DTT], 0.01% bromophenol blue, 4% sodium dodecyl sulfate [SDS], 20% glycerol). On ice, cell lysates were briefly sonicated once for 5 seconds at 40% amplitude output followed by 25 minutes heating at 95 °C. Afterwards, cell lysates were briefly centrifuged at 13,000 × g at room temperature for 1 minute. Then, 20  $\mu$ l of cell lysates were separated on 4-12% tris-glycine SDS-polyacrylamide gel electrophoresis (SDS-PAGE) from Invitrogen, and transferred to methanol-soaked polyvinylidene difluoride (PVDF) membranes from Millipore. Membranes were blocked in PBS buffer supplemented with 0.1% TWEEN 20 and 5% skim milk (PBS-T), and incubated for 1 hour at room temperature under gentle horizontal shaking. Afterwards, membranes were incubated overnight at 4°C with the primary antibodies under gentle horizontal shaking. The primary antibodies were prepared in PBS-T with the following dilutions: anti-KDM4B (1:1000), anti-PAX3-FOXO1 (1:200), anti-FOXO1 (1:1000), anti-Hsp90 (1:1,000), anti-actin (1:5,000), anti-total H3 (1:2,000), anti-H3K4me3 (1:2,000), anti-H3K9me3 (1:2,000) and anti-H3K36me3 (1:2,000). Next day, membranes were washed 3 times (each wash for 5 minutes) with PBS-T at room temperature. Protected from light, membranes were then incubated with goat anti-mouse or goat anti-rabbit HRP-conjugated secondary antibodies (1:5,000) for 1 hour at room temperature. Then, membranes were washed 3 times (each wash for 5 minutes) with PBS-T at room temperature. Lastly, membranes were incubated for 1 minute at room temperature with SuperSignal West Pico PLUS Chemiluminescent Substrate (34580, Thermo Fisher Scientific), and the bound antigen-antibody complexes were visualized using Odyssey Fc Imaging System (LI-COR Corp., Lincoln, NE).

### **Immunoprecipitation**

Cells were washed twice with ice-cold PBS and then directly lysed on ice with co immunoprecipitation (co-IP) buffer (25 mM Tris-HCl [pH 7.5], 150 mM NaCl, 1 mM ethylenediaminetetraacetic acid [EDTA], 1% nonyl phenoxyethoxyethanol [NP40], 5% glycerol) supplemented with phosphatase (Roche) and protease (Roche) inhibitor cocktails. The cell lysate was transferred to a 2-ml Eppendorf tube, and incubated on ice for 15 minutes, and vortexed every 5 minutes. Then, the cell lysate was centrifuged at 13,000 × g at 4 °C for 15 minutes. The pre-cleared supernatant was incubated with rotation at 4 °C overnight with 4 µg of anti-HSP90 and 4 µg of anti-normal IgG as a negative control. Next day, 50 µl of protein A/G magnetic beads (88802, Thermo Scientific Fisher) were washed 3 times at room temperature with the co-IP buffer, and then added to each pre-cleared supernatant for 1 hour incubation with rotation at 4 °C. Afterwards, the supernatant (flow-through) was discarded; the beads were washed 3 times with co-IP buffer, eluted with 50 µl of the 2X sample loading buffer and heated for 10 mins at 95 °C. Input lysate was heated for 25 mins at 95 °C. 20 µl of co-IP and 20 µl of input reactions were subjected to SDS-PAGE and immunoblotting with anti-Hsp90 and anti-PAX3-FOXO1 antibodies (as described above).

### **Immunohistochemistry**

Xenografts were fixed in 10% neutral buffered formalin, embedded in paraffin, sectioned at 4 µm, stained with hematoxylin and eosin and reviewed by light microscopy using an upright Nikon Eclipse Ni microscope (Nikon Instruments, Inc.). Immunohistochemistry was performed on 4 µm thick tissue sections mounted on positively charged glass slides (Superfrost Plus; Thermo Fisher Scientific, Waltham, MA), and dried at 60°C for 20 minutes. The procedures for immunohistochemistry were performed using a Ventana DISCOVERY ULTRA autostainer (Roche). Heat induced epitope retrieval was applied for 1 hour using cell conditioning 1 buffer (CC1, Roche, #950-500) followed by the application of anti-CD31 (Histobiotec, DIA-310, 1:50) or anti-Cleaved Caspase 3 (BioCare Medical, CP229C, 1:500) for 32 minutes. The following reagents were used for visualization: DISCOVERY OmniMap anti-Rat HRP (Roche,760-4457) for CD31 or OmniMap anti-Rabbit HRP (Roche, 760-4311) and the DISCOVERY ChromoMap DAB kit (Roche, 760-159), which was applied for 8 min at room temperature. Tissues were counterstained with Hematoxylin II (Roche, 790-228) for 12 min and Bluing reagent (Roche, 760-2037) for 4 min as a post-counterstain procedure. TUNEL was performed using the *In situ* Cell Death Detection Kit (Roche, 11684817910) according to the manufacturer's instructions. The quantification of Caspase 3, TUNEL and CD31 was performed using ImageJ IHC tool box (for

Caspase 3 and TUNEL) and Vessel Analysis plug in program (for CD31), and unpaired student t test was used to compare the difference between vehicle and treatment.

### **Chromatin immunoprecipitation**

$1 \times 10^7$  of RH30 cells treated with DMSO control or  $1 \mu\text{M}$  of Geldanamycin for 24 h were cross-linked with fresh prepared 1% formaldehyde (final concentration) for 10 min and quenched with 125 mM glycine for 5 min at room temperature. Cells were washed once with Dulbecco's Phosphate-Buffered Saline (DPBS). 5-8 ml of cold Cell lysis buffer (5 mM PIPES pH 8.0, 85 mM KCl, 0.5% NP-40 with 1 tablet protease inhibitor cocktail) were added to plate after removing DPBS. The cells were scraped with a cell scraper and transfer into 50-ml conical tubes on ice. Cell pellets were collected by centrifuging at 2,000 rpm for 5 minutes at  $4^\circ\text{C}$ . The pellets were resuspended in cell lysis buffer and incubated on ice for 10 min. Cells were passed through a 20-gauge needle 20 times. The nuclei were collected by centrifuging at 2,000 rpm at  $4^\circ\text{C}$  for 5 minutes. The nuclear pellets were resuspended and lysed with 250  $\mu\text{L}$  RIPA buffer (1X PBS, 1% NP-40, 0.5% sodium deoxycholate, 0.1% SDS with 1 tablet protease inhibitor cocktail). The lysates were sonicated for at least 30 min (30 sec on / 30 sec off) using Bioruptor Pico (Diagenode, Inc., Denville, NJ) and centrifuged at 14,000 rpm in a microfuge for 15 minutes at  $4^\circ\text{C}$ . The supernatant was collected and the sonicated DNA fragments were examined by electrophoresis on a 1% agarose gel. The sonicated samples with enrichment of fragments between the 100 to 500 bp range were used for the chromatin immunoprecipitation (ChIP) after removing 50  $\mu\text{L}$  from each sample as input. The primary antibodies H3K9me3 (Millipore, 07-442) and H3K36me3 (RevMab, 31-1051-00) were coupled with 25  $\mu\text{L}$  magnetic beads (Dynabeads M-280 Sheep Anti-Rabbit IgG, Invitrogen 11203D) overnight in the cold room at  $4^\circ\text{C}$ , washed three times with PBS/BSA (1XPBS / 5 mg/ml BSA (fraction V)) at  $4^\circ\text{C}$ , then incubated with sonicated DNA chromatin samples overnight in the cold room at  $4^\circ\text{C}$ . The beads containing immuno-bound chromatin were collected by placing the microfuge tube on a magnet rack. The beads were extensively washed with LiCl wash buffer (100 mM Tris pH 7.5 / 500 mM LiCl / 1% NP-40 / 1% sodium deoxycholate) 5 times and TE Buffer (10 mM Tris-HCl pH 7.5 / 0.1 mM Na<sub>2</sub>EDTA) once. Bound chromatin was eluted by IP Elution Buffer (1 % SDS / 0.1 M NaHCO<sub>3</sub>) and reverse-crosslinked at  $65^\circ\text{C}$  overnight. DNAs were purified using Min-Elute PCR purification kit (Qiagen, Valencia, CA) after the treatment of RNase A and proteinase K. ChIP enrichment DNAs were submitted to library preparation and sequencing. ChIP-seq library preparation and sequencing were carried out by the Hartwell Center at St Jude Children's Research Hospital. Briefly, 5-10 ng of DNA was used to prepare libraries by the NEBNext ChIP-Seq Library Prep Reagent Set for

Illumina with NEBNext Q5 Hot Start HiFi PCR Master Mix according to the manufacturer's instructions (New England Biolabs). Completed ChIP-seq libraries were analyzed for insert size distribution using a 2100 BioAnalyzer High Sensitivity kit (Agilent) or Caliper LabChip GX DNA High Sensitivity Reagent Kit (Perkin Elmer). All libraries were quantified using the Quant-iT PicoGreen dsDNA assay (Life Technologies), Kapa Library Quantification kit (Kapa Biosystems). Fifty-cycle single-end sequencing was performed using an Illumina HiSeq 2500 or HiSeq 4000.

### **ChIP-seq analysis**

Mapping reads and visualizing data. The ChIP-seq raw reads were aligned to the human reference genome (hg19) using BWA (version 0.7.12; default parameter) to and then marked duplicated reads with Picard (version 1.65), with only nonduplicated reads kept by samtools (version 1.3.1, parameter “-q 1 -F 1024”). To control the quality of the data and estimate the fragment size, the nonduplicated version of SPP (version 1.11) was used to calculate relative strand correlation value with support of R (version 3.5.1). To visualize ChIP-seq data on integrated genome viewer (IGV) (version 2.3.82), we used genomeCoverageBed (bedtools 2.25.0) to produce genome-wide coverage in BEDGRAPH file and then converted it to bigwig file by bedGraphToBigWig. The bigwig files were scaled to 15 million reads to allow comparison across samples.

Peak calling, annotation and motif analysis. MACS2 (version 2.1.1) was used to call narrow peaks (H3K27Ac and H3K4me3) with option “nomodel” and “extsize” defined as fragment size estimated by SPP, FDR corrected p value cutoff 0.05. For broad peaks (H3K9me3, H3K36me3, H3K27me3, and H3K4me1), SICER (version 1.1, with parameters of redundancy threshold 1, window size 200bp, effective genome fraction 0.86, gap size 600bp, FDR 0.00001 with fragment size defined above) has been used for domain calling. Enriched regions were identified by comparing the IP library file to input library file. Peak regions were defined to be the union of peak intervals in replicates from control or treated cells respectively. Promoters were defined as mouse RefSeq TSS  $\pm$  1000bp regions. Genomic feature annotation of peaks was done by annotatePeaks.pl, a program from HOMER suite (v4.8.3, <http://homer.salk.edu/homer/>). The HOMER software was used to perform de novo motif discovery as well as check the enrichment of known motifs in a set of given peaks.

Differential analysis. ChIP-seq raw read counts were reported for each region/each sample using bedtools 2.25.0. Raw read counts were voom normalized and statistically contrasted using the R(version 3.5.1) packages limma and edgeR (version 3.16.5) for CPM calculation and differential

analysis. An empirical Bayes fit was applied to contrast treated samples to control samples and to generate log fold changes, p values and false discovery rates for each peak region.

### **Animal experiments**

All murine experiments were done in accordance with a protocol approved by the Institutional Animal Care and Use Committee of St. Jude Children's Research Hospital. Subcutaneous xenografts in Figure 5 and Figure 6E were established in CB17 severe combined immunodeficient mice (CB17 *scid*, Taconic) by implanting  $5 \times 10^6$  cells in Matrigel. Subcutaneous xenografts in Figure 6A - 6D were established NOD.Cg-*Prkdc<sup>scid</sup>*, *Il2rg<sup>tm1Wjl</sup>*/SzJ (NOD *scid* gamma, NSG) mice by implanting  $5 \times 10^6$  cells in Matrigel. Tumor measurements were done weekly using electronic calipers, and volumes calculated as  $\pi/6 \times d^3$  where  $d$  is the mean of two diameters taken at right angles. Subcutaneous xenografts were treated with 25 mg/kg of 17-DMAG or 50 mg/kg of 17-AAG via intraperitoneal injection twice daily, every four days. 17-DMAG was dissolved in 1% DMSO, 1% TWEEN<sup>®</sup> 80 (#P4780 from Sigma), 30% PEG300 (#202371 from Sigma) and 68% ddH<sub>2</sub>O. 17-AAG was dissolved in 5% DMSO and 95% corn oil. Vincristine was administered in a dose of 0.38 mg/kg via IP injection once daily every week. Vincristine was dissolved in 100% saline. Irinotecan was administered in a dose of 1.25 mg/kg via IP injection once daily, for 5 days on and 2 days off schedule. Irinotecan was dissolved in 5% DMSO and 95% saline. Mice were sacrificed because of an adverse event before they had completed 14d and were removed from the data set. Tumor response: For individual mice, progressive disease (PD) was defined as < 50% regression from initial volume during the study period and > 25% increase in initial volume at the end of study period. Stable disease (SD) was defined as < 50% regression from initial volume during the study period and  $\leq$  25% increase in initial volume at the end of the study. Partial response (PR) was defined as a tumor volume regression  $\geq$  50% for at least one time point but with measurable tumor ( $\geq 0.10 \text{ cm}^3$ ). Complete response (CR) was defined as a disappearance of measurable tumor mass ( $< 0.10 \text{ cm}^3$ ) for at least one time point.

### **Statistical analysis**

To determine statistical significance, the unpaired, two-tailed Student  $t$  test was calculated using the  $t$  test calculator available on GraphPad Prism 8.0 software. A  $p$  value of less than 0.05 was considered statistically significant. Kaplan-Meier survival analysis was calculated using log-rank (Mantel-Cox) method in GraphPad Prism 8.0 software.

The Kruskal Wallis test was utilized to determine if there was a statistically significant different among the 4 treatment groups at each time point. The exact Wilcoxon Rank Sum test was utilized

to determine if there was a statistically significant difference between receiving one treatment vs receiving the combination treatment. All statistical analyses were conducted in SAS 9.4 and a two-sided significance level of  $p < 0.05$  was determined a priori.